Strong Form Meshfree Collocation Method for Higher Order and Nonlinear PDEs in Engineering Applications

Andrew Christian Beel

B.S., University of Colorado Boulder, 2019

A thesis submitted to the Faculty of the Graduate School of the

University of Colorado Boulder

in partial fulfillment of the requirement for the degree of

Master of Science

Department of Civil, Environmental and Architectural Engineering

2019

This thesis entitled:

Strong Form Meshfree Collocation Method for Higher Order and Nonlinear PDEs in Engineering Applications

written by Andrew Christian Beel

has been approved for the Department of Civil, Environmental and Architectural Engineering

---

Dr. Jeong-Hoon Song (Committee Chair)

Dr. Ronald Pak

Dr. Victor Saouma

Dr. Richard Regueiro

Date

The final copy of this thesis has been examined by the signatories, and we find that both the content and the form meet acceptable presentation standards of scholarly work in the above mentioned discipline.

Abstract

Andrew Beel (M.S., Civil Engineering, Department of Civil, Environmental and Architectural Engineering)

Strong Form Meshfree Collocation Method for Higher Order and Nonlinear PDEs in Engineering Applications

Thesis directed by Assistant Professor Jeong-Hoon Song

The strong form meshfree collocation method based on Taylor approximation and moving least squares is an alternative to finite element methods for solving partial differential equations in engineering applications. This study examines how the proposed alternative method solves (i) higher-order and (ii) nonlinear partial differential equations. First, the proposed method is formulated in Chapter 2 for the general discretization and solution of strong forms of partial differential equations. Chapter 3 presents the convergence and error behavior of the proposed method for the fourth-order Stommel–Munk equation for wind-driven ocean circulation, as well as the numerical solution of this equation on a domain of more realistic geometry representing the Mediterranean Sea. In Chapter 4, the proposed method is used to solve the nonlinear equations governing linear elastic, small-deformation multi-body thermomechanical contact, including a comparison with analytical and finite element solutions for three verification problems.

Acknowledgments

First, I would like to thank Dr. J.H. Song for all his academic and personal guidance. His kindness, attention to detail, and encouragement of independent thought and research have changed my life. No matter the circumstances, Dr. Song has always been loyal and committed to my success and that of his other students. I hope to live up to his example of hard work, self-reliant problem solving, quality research, and excellent teaching ability.

I would also like to thank Dr. Ron Pak for his personal mentorship. His emphasis on what really matters in research—such as the intrinsic value of knowledge, thoroughly verifying and validating theories, and making broader impacts—has greatly shaped my philosophy.

I am grateful to my committee members for their guidance on this thesis. It has been an honor to share my work with them! Also, I could not have done this work without Dr. T.Y. Kim, Dr. John Michopoulos and his team, and Dr. Jim Curry. Their warm personalities, high standards of quality, and practical understanding of the business of research have made me a better person and researcher.

Finally, I am forever indebted to my parents for their superhuman patience and understanding and unconditional love. I love you, Mom and Dad!

Contents

List of Tables

List of Figures

Chapter 1

Introduction

Higher-order and nonlinear partial differential equations (PDEs) arise in many engineering applications. For example, the PDEs governing Kirchhoff-Love plates and thin shells are higher-order since they contain fourth-order spatial derivative terms [1]. Similarly, the Cahn-Hilliard phase-field equation describing spontaneous separation of the components of a binary fluid contains a biharmonic term, which is also of fourth order [2]. Nonlinear PDEs are ubiquitous, arising for example in any study of inelasticity via material plasticity and large deformation [3]. Engineers need reliable numerical methods to solve the PDEs arising in such applications.

Most of the computational studies of higher-order and nonlinear partial differential equations in mechanics make use of the finite element method (FEM). However, the FEM has disadvantages related to dependency on a mesh and complications arising from use of the weak form, particularly in the context of higher-order and nonlinear PDEs in mechanics. For example, to use the FEM for higher-order PDEs, the governing equations must be decomposed into systems of lower-order PDEs. FEM solution of the corresponding weak forms require higher-order polynomial shape functions and global continuity of the numerical solution, which results in higher computational cost [4]. In nonlinear problems involving material or contact interfaces or other discontinuities, FEM domain integration with standard quadra-

ture techniques becomes difficult and special modifications must be made to alleviate these difficulties [5]. In particular, for contact problems, special techniques must be developed to overcome the possibility of element node-to-segment contact [6].

Weak form-based meshfree methods such as the element-free Galerkin method have been developed to alleviate some of the difficulties associated with the FEM [7]. Other interesting weak form-based meshfree methods can be found in [8, 9, 10]. Although these methods eliminate mesh dependency, they still require domain integration and exact computation of derivatives, which increases computational cost. Due to these difficulties, it is worth exploring other numerical methods for solving higher-order and nonlinear partial differential equations.

1.1 An alternative method

An alternative to both traditional FEM and weak form-based meshfree methods is the strong form-based meshfree point collocation method. The particular variation of this alternative considered here, based on Taylor approximation and moving least squares (MLS), was first developed in [11, 12, 13, 14, 15]. By directly discretizing the strong form of governing PDEs using a set of approximate derivative operators, the proposed method avoids mesh dependency, domain integration, and exact computation of derivatives [5]. In addition, the proposed method easily treats boundary conditions and adaptive refinement. Motivated by these advantages, the method has been successfully applied to various problems such as incompressible fluid flows [14], elastic crack problems [16], and the asymptotic crack tip singularity in a linear elastic fracture [17, 18]. Later, the method was applied to weak and strong discontinuities [5, 19, 20], diffusive interface modeling and stress analysis [21, 22, 23], and inelastic material problems [24].

Despite the advantages originating from the flexibility in discretization, the strong form-based meshfree collocation method also exhibits drawbacks. For instance, since the proposed

method is based on the strong form, it lacks the corresponding advantages of methods based on variational forms, e.g., accuracy of solutions in the sense of total energy and some of the well-developed mathematical framework for analyzing error behavior. The proposed method also struggles with instabilities and sensitivity to numerical parameters. While a more thorough analysis of these drawbacks is needed to evaluate the proposed method, an in depth discussion about the stability of a similar meshfree method can be found in [25].

In view of the advantages and challenges associated with the proposed method, the present study seeks to demonstrate how the proposed method may be used to solve higher-order and nonlinear PDEs. The higher-order PDE considered in this study arises in the context of wind-driven ocean circulation, while the nonlinear PDEs considered in this study arise in the context of multi-body thermomechanical contact.

1.2 Higher-order PDEs in wind-driven ocean circulation

The equations describing wind-driven ocean circulation contain higher-order spatial derivative terms and are therefore of interest in this study. Understanding large scale wind-driven ocean circulation at mid-latitude is important to predict weather, including extreme events such as cyclones [26]. Common features of wind-driven ocean flows are strong western boundary currents, weak interior flows, and weak eastern boundary currents, as in the north Atlantic and Pacific oceans. Popular mathematical models to capture these phenomena are the quasi-geostrophic equations (QGE), the Stommel model, and the Stommel–Munk model [27, 28]. Whereas the QGE are time-dependent nonlinear partial differential equations (PDEs), the Stommel model and the Stommel–Munk model are stationary linear PDEs.

Existing numerical methods that can be employed to solve these mathematical models are the finite difference method (FDM) [29], finite volume method (FVM) [30, 31], and the FEM [32, 33, 34]. For geophysical flows, the FVM is particularly appealing due to its capability of

unstructured grids along with preserving conservation properties of the underlying equations. On the other hand, advantages of the FEM over the FDM are an easy treatment of complex boundaries and grid refinement to achieve a high accuracy in regions of interest. Because FEM techniques have achieved optimal rates of convergence for the equations formulated based on the streamfunction, recent developments of numerical techniques have focused on the streamfunction formulation [35]. Examples include a conforming Galerkin formulation using C^1-elements [35], a discontinuous Galerkin formulation using C^0-elements [36], and B-spline based FEM formulations [37, 38, 39]. Further development of the B-spline based FEM was achieved by introducing an adaptivity technique for the Stommel and Stommel–Munk models [40] and modeling arbitrary shaped coastal boundaries on embedded boundaries [41].

In the context of wind-driven oceanic flow simulation, it is challenging to achieve accurate and efficient computational models in light of the complex boundaries of arbitrarily shaped coastlines. Furthermore, capturing a strong western boundary layer requires an efficient adaptive refinement technique. In handling arbitrarily shaped coastlines and strong western boundary layers, the computational cost of a conforming Galerkin formulation using C^1-elements is relatively expensive. Using B-splines, modeling arbitrary shape geometries often involves either a mapping (as in isogeometric analysis [42]) or a fictitious-domain approach [43]. Moreover, B-splines have difficulty in applying boundary conditions, particularly in the case of a strong boundary layer [44].

Unlike the other methods described here, the proposed strong form meshfree collocation method provides a straightforward way to approximate higher-order derivatives and apply boundary conditions. Thus, it represents a compelling alternative or complement to these other methods for solving the equations governing wind-driven ocean circulation and for higher-order PDEs in general. In Chapter 3 of this study, the proposed method is used to solve the linear second-order Stommel and fourth-order Stommel–Munk equations for various forcing terms. An error analysis is conducted for the verification examples presented, including a brief discussion of stability and sensitivity to numerical parameters. Finally,

the method is used to solve the Stommel–Munk equation on a polygon representing the Mediterranean Sea, demonstrating the method's potential to solve more realistic problems involving higher-order PDEs.

1.3 Nonlinear PDEs in thermomechanical contact

The second application of the proposed method presented here is linear elastic, small-deformation multi-body thermomechanical contact. Although the mechanical and thermal equilibrium equations are linear under these assumptions, the constraints on the mechanical and thermal fields at the contact surface introduce nonlinear equations in displacement and temperature, making the overall problem nonlinear. Thermomechanical contact has wide-ranging applications in engineering, from modeling automobile crash safety to hip joint replacements to pellet-cladding interactions in a nuclear fuel rod [6, 45, 46].

In many of these applications, coupling between the mechanical and thermal fields is an important concern. For example, temperature changes may cause significant thermal expansion, mechanical friction may generate significant heat, and degree of heat transfer across contact surfaces may depend significantly on the contact pressure [6, 47]. Two general approaches used to handle this coupling in a computational context are a staggered (loose coupling) and a monolithic (tight coupling) approach. In each step of a staggered scheme, the displacement and temperature fields are assumed to be fixed with respect to each other, and both fields are adjusted individually in a fixed-point iteration until both converge. In contrast, a monolithic scheme considers all interactions between thermal and mechanical fields within one iteration and solves one system of equations including all solution variables [48]. In general, a staggered approach is more likely to be successful if displacement due to thermal expansion is expected to be small compared to displacement due to mechanical loading. In contrast, a monolithic scheme would be more appropriate when thermal expansion is significant. Other researchers have explored both monolithic and staggered approaches

for thermoelasticity and thermomechanical contact problems. For example, a monolithic approach was used in [49] to model thermo-structure interaction and applied to examples related to behavior of rocket nozzles. In [50], an unconditionally stable staggered scheme was developed for use in time-dependent thermoelasticity problems.

Over the last three decades, advances in computational contact mechanics have mainly involved finite element methods that use special techniques to model contact interfaces and handle associated constraints. For example, Papadopoulos and Taylor [51] developed a mixed finite element method for contact problems. Wriggers and Miehe [52] developed a finite element method for large deformation thermomechanical contact. Another popular approach to solving contact problems is the mortar finite element method. This method was developed, for example, in [53] and used in [54, 55, 56, 57, 58, 59] for various contact problems.

In contrast to the other methods described here, the proposed method is meshfree and allows for easy treatment of the contact interface. Also unlike the FEM, for which element node-to-segment contact is a concern [6], ensuring pairs of corresponding contact nodes is straightforward because new collocation points are easily added on the contact boundary as needed. Due to this and other advantages, the proposed method has promise to be useful for contact mechanics problems. In Chapter 4 of this study, a formulation of the proposed method for thermomechanical contact is presented using a staggered Newton-Raphson approach. Then, numerical solutions are presented for three verification problems, including frictional contact along an inclined contact surface, smooth and frictional contact between two half-cylinders, and thermomechanical contact between two rectangular blocks. The numerical solutions presented are compared with analytical or FEM solutions for verification.

Chapter 2

Strong Form Meshfree Point Collocation Method

This chapter develops the proposed strong form meshfree collocation method for solving partial differential equations. The material in this chapter is adapted from [4].

The meshfree point collocation method presented here allows the construction of numerical derivative operators that are used to discretize the strong form of PDEs. We consider a plane domain Ω in n-space. Let $\boldsymbol{\alpha} = \{\alpha_1, \alpha_2, ..., \alpha_n\}$ be an n-dimensional array of nonnegative integers and define $|\boldsymbol{\alpha}| \cong \Sigma_{i=1}^{n} \alpha_i$. Let $\mathbf{x} = \{x_1, x_2, ..., x_n\}^T$ be an n-dimensional vector. Then, we write

$$\mathbf{x}^{\boldsymbol{\alpha}} = \prod_{i=1}^{n} x_i^{\alpha_i} \quad \text{and} \quad \boldsymbol{\alpha}! = \prod_{i=1}^{n} \alpha_i!. \tag{2.1}$$

For convenience, such an array of nonnegative integers $\boldsymbol{\alpha}$ will be referred to as an exponent array from this point forward.

Given a function $u(\mathbf{x}) \in \mathcal{C}^m(\Omega)$ for a nonnegative integer m, we write the αth derivative of $u(\mathbf{x})$ as

$$D_{\mathbf{x}}^{\boldsymbol{\alpha}} u = \frac{\partial^{|\boldsymbol{\alpha}|} u}{\partial x_1^{\alpha_1} \partial x_2^{\alpha_2} \cdots \partial x_n^{\alpha_n}} \tag{2.2}$$

for $|\boldsymbol{\alpha}| \leq m$. With this notation, the mth-order Taylor expansion P_m of u, centered at $\mathbf{y}$

and evaluated at $\mathbf{x}$, is given by

$$P_m(\mathbf{x};\mathbf{y}) = \sum_{|\boldsymbol{\alpha}|\leq m} \frac{(\mathbf{x}-\mathbf{y})^{\boldsymbol{\alpha}}}{\boldsymbol{\alpha}!} D^{\boldsymbol{\alpha}}_{\mathbf{x}} u(\mathbf{y}). \tag{2.3}$$

Recall that we seek a way to construct numerical derivative operators. The first step is to order all derivatives of $u(\mathbf{y})$ of up to order m in n variables and arrange them in a vector $\mathbf{a}(\mathbf{y})$. Note that there are $L = (m+n)!/(m!n!)$ such derivatives. This vector is constructed by placing all derivatives of each degree in lexicographical order, and then ordering these partial lists in order of increasing degree. This ordering is chosen so that the position of the $\boldsymbol{\alpha}_k$ entry of the polynomial vector is the same as that of the corresponding entry of Pascal's triangle. An advantage of this ordering is that the order of magnitude of the entries generally decreases from the first to last entry, which facilitates scaling of the moment matrix $\mathbf{M}$ described below for improvement of the condition number. For clarity, an example of this derivative ordering is given in Table 2.1.

Table 2.1: Entries of $\mathbf{a}(\mathbf{y})$ and $\mathbf{p}(\mathbf{x};\mathbf{y})$ for $m = 4$, $n = 2$, and $L = 15$ ($0 \leq i \leq m$ and $0 \leq k \leq L$)

i	k	$\boldsymbol{\alpha}_k$	Entries of $\mathbf{a}(\mathbf{y})$	Entries of $\mathbf{p}(\mathbf{x};\mathbf{y})$
0	1	$(0,0)$	$u(\mathbf{y})$	1
1	2	$(1,0)$	$u_{y_1}(\mathbf{y})$	$x_1 - y_1$
	3	$(0,1)$	$u_{y_2}(\mathbf{y})$	$x_2 - y_2$
2	4	$(2,0)$	$u_{y_1y_1}(\mathbf{y})$	$(x_1-y_1)^2/2$
	5	$(1,1)$	$u_{y_1y_2}(\mathbf{y})$	$(x_1-y_1)(x_2-y_2)$
	6	$(0,2)$	$u_{y_2y_2}(\mathbf{y})$	$(x_2-y_2)^2/2$
3	7	$(3,0)$	$u_{y_1y_1y_1}(\mathbf{y})$	$(x_1-y_1)^3/6$
	8	$(2,1)$	$u_{y_1y_1y_2}(\mathbf{y})$	$(x_1-y_1)^2(x_2-y_2)/2$
	9	$(1,2)$	$u_{y_1y_2y_2}(\mathbf{y})$	$(x_1-y_1)(x_2-y_2)^2/2$
	10	$(0,3)$	$u_{y_2y_2y_2}(\mathbf{y})$	$(x_2-y_2)^3/6$
4	11	$(4,0)$	$u_{y_1y_1y_1y_1}(\mathbf{y})$	$(x_1-y_1)^4/24$
	12	$(3,1)$	$u_{y_1y_1y_1y_2}(\mathbf{y})$	$(x_1-y_1)^3(x_2-y_2)/6$
	13	$(2,2)$	$u_{y_1y_1y_2y_2}(\mathbf{y})$	$(x_1-y_1)^2(x_2-y_2)^2/4$
	14	$(1,3)$	$u_{y_1y_2y_2y_2}(\mathbf{y})$	$(x_1-y_1)(x_2-y_2)^3/6$
	15	$(0,4)$	$u_{y_2y_2y_2y_2}(\mathbf{y})$	$(x_2-y_2)^4/24$

Let $\boldsymbol{\alpha}_k$ be an exponent array like the one characterized by (2.1), with the property that

the jth entry of $\boldsymbol{\alpha}_k$ equals the number of derivatives of $u(\mathbf{y})$ with respect to y_j taken when evaluating the kth element of $\mathbf{a}(\mathbf{y})$. In other words, $\boldsymbol{\alpha}_k$ is the exponent array that makes the kth entry of $\mathbf{a}(\mathbf{y})$ equal to $D_{\mathbf{y}}^{\boldsymbol{\alpha}_k} u$. For a given m, this exponent array may be used to construct a polynomial vector $\mathbf{p}(\mathbf{x};\mathbf{y})$ with kth entry given by

$$p_k(\mathbf{x};\mathbf{y}) = \frac{(\mathbf{x}-\mathbf{y})^{\boldsymbol{\alpha}_k}}{\boldsymbol{\alpha}_k!} \tag{2.4}$$

and corresponding to the kth entry of $\mathbf{a}(\mathbf{y})$ so that the Taylor polynomial in (2.3) may be rewritten as

$$P_m(\mathbf{x};\mathbf{y}) = \mathbf{p}(\mathbf{x};\mathbf{y})^T \mathbf{a}(\mathbf{y}). \tag{2.5}$$

For better understanding, the exponent arrays and entries of $\mathbf{p}(\mathbf{x};\mathbf{y})$ and $\mathbf{a}(\mathbf{y})$ for $m = 4$ and $n = 2$ are given in Table 2.1.

Next, the method of moving least squares is used in conjunction with the Taylor expansion above to formulate discrete derivative operators. For a set of N points $\mathbf{x}_J$ $(J = 1, 2, ..., N)$ in Ω, we seek to minimize the discrete weighted residual functional

$$\mathcal{F}\left[\mathbf{a}(\mathbf{y})\right] = \sum_{J=1}^{N} w\left(\frac{\mathbf{x}_J - \mathbf{y}}{\rho(\mathbf{y})}\right)\left[\mathbf{p}(\mathbf{x}_J;\mathbf{y})^T \mathbf{a}(\mathbf{y}) - u_J\right]^2 \tag{2.6}$$

with respect to $\mathbf{a}(\mathbf{y})$. Here, w is a weight function and $\rho(\mathbf{y})$, termed the dilation parameter, is the radius of a ball around $\mathbf{y}$ called the compact support. Outside of this radius, the weight function is set to zero. The dilation parameter need not be constant over the domain; rather, it should be smaller in areas of local refinement and larger along boundaries. An illustration of the dilation parameter is given in Figure 2.1. In this illustration, the dilation parameter was computed as the distance between each center node and the farthest away of its 60 nearest neighbors.

For a fixed $\mathbf{y}$, $\mathcal{F}[\mathbf{a}(\mathbf{y})]$ is minimized for a unique $\mathbf{a}(\mathbf{y})$ for which $\partial\mathcal{F}/\partial\mathbf{a} = 0$ because $\mathcal{F}$ is nonnegative and quadratic in $\mathbf{a}$. If the local center is moved (hence the term moving

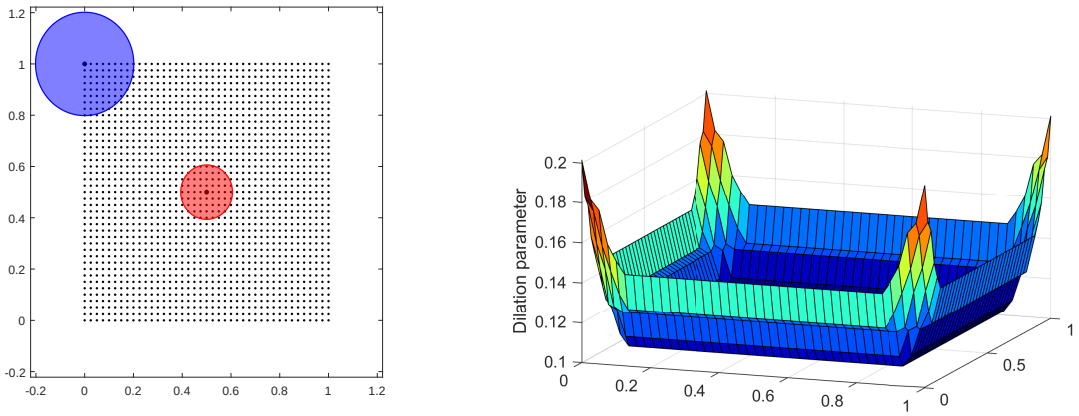

(a) (b)

Figure 2.1: For a uniform grid of collocation points, (a) examples of compact support domains and (b) a surface plot of the dilation parameter are given for a search of the 60 nearest neighbors of each point

least squares) to each point $\mathbf{x}$ at which a set of derivative operators is desired, then the local $\mathcal{F}[\mathbf{a}(\mathbf{x})]$ is minimized by the $\mathbf{a}(\mathbf{x})$ for which $\partial\mathcal{F}/\partial\mathbf{a} = 0$. In other words, minimizing (2.6) and taking $\mathbf{y} \to \mathbf{x}$ results in

$$\mathbf{a}(\mathbf{x}) = \mathbf{M}^{-1}(\mathbf{x})\mathbf{B}(\mathbf{x})\mathbf{u} \tag{2.7}$$

where $\mathbf{u} = \{u_1, u_2, ..., u_N\}^T$ is the nodal solution vector for the N points in Ω, and $\mathbf{M}$ and $\mathbf{B}$ are given by

$$\mathbf{M}(\mathbf{x}) = \sum_{J=1}^{N} \left(\mathbf{p}(\mathbf{x}_J; \mathbf{x}) w \left(\frac{\mathbf{x}_J - \mathbf{x}}{\rho(\mathbf{x})} \right) \mathbf{p}^T(\mathbf{x}_J; \mathbf{x}) \right) \tag{2.8}$$

and

$$\mathbf{B}(\mathbf{x}) = \left[w \left(\frac{\mathbf{x}_1 - \mathbf{x}}{\rho(\mathbf{x})} \right) \mathbf{p}(\mathbf{x}_1; \mathbf{x}), w \left(\frac{\mathbf{x}_2 - \mathbf{x}}{\rho(\mathbf{x})} \right) \mathbf{p}(\mathbf{x}_2; \mathbf{x}), ..., w \left(\frac{\mathbf{x}_N - \mathbf{x}}{\rho(\mathbf{x})} \right) \mathbf{p}(\mathbf{x}_N; \mathbf{x}) \right]. \tag{2.9}$$

Note that the cost of computing derivatives of shape functions is replaced by that of inverting N $\mathbf{M}$ matrices, each of which is only $L \times L$. Also, since the method uses a diffuse derivative approximation, computation of these derivative operators does not require exact differentiation of shape functions or of the weight function, so there is no differentiability requirement for either. Examples of non-smooth weight functions are plotted in Figure 2.2

and given by

$$\begin{aligned} w(\mathbf{r}) &= (1 - ||\mathbf{r}||)^4 \qquad \text{(4th-order)} \\ w(\mathbf{r}) &= (1 - ||\mathbf{r}||^{\frac{1}{2}})^2 \qquad \text{(root power)} \end{aligned} \tag{2.10}$$

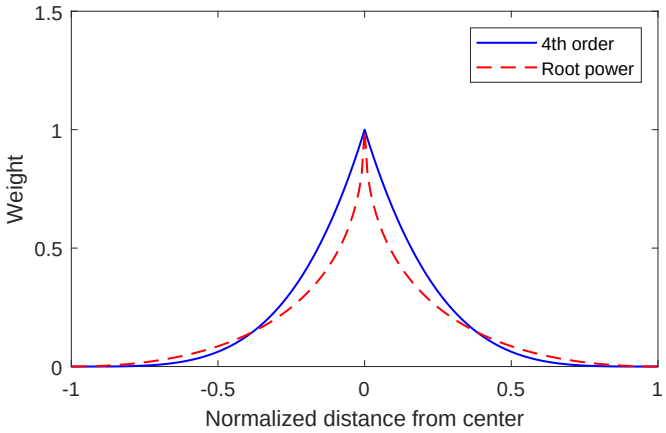

Figure 2.2: Examples of non-smooth weight functions

An important consequence of this result is that the kth entry of $\mathbf{a}(\mathbf{x}) = \mathbf{M}^{-1}(\mathbf{x})\mathbf{B}(\mathbf{x})\mathbf{u}$ gives approximation for the $\boldsymbol{\alpha}_k$th derivative of u at $\mathbf{x}$. Thus, for each $\mathbf{x}_I \in \mathbf{x}_1, \mathbf{x}_2, ..., \mathbf{x}_N$, we can define differential operators $\boldsymbol{\Phi}_I^{\boldsymbol{\alpha}_k}$ defined to be the kth row of $\mathbf{M}^{-1}(\mathbf{x}_I)\mathbf{B}(\mathbf{x}_I)$, i.e.,

$$\boldsymbol{\Phi}_I^{\boldsymbol{\alpha}_k}\mathbf{u} \approx D_{\mathbf{x}}^{\boldsymbol{\alpha}_k} u(\mathbf{x}_I) \tag{2.11}$$

Using (2.11), all differential operators in the strong form of PDEs and their boundary conditions can be discretized for any set of N collocation points in $\bar{\Omega}$.

Chapter 3

Wind-driven Ocean Circulation

This chapter, which is largely reproduced from [4], examines how the proposed method is used to solve higher order PDEs. The PDEs of interest in this study are the linearized quasi-geostrophic equations used to model wind-driven ocean circulation, namely the second-order Stommel and fourth-order Stommel–Munk equations. Section 3.1 describes these equations and their boundary conditions, as well as how the proposed method is used to discretize these equations. Section 3.2 presents the results of solving the Stommel and Stommel–Munk equations, including numerical experiments of convergence behavior. The final numerical example, the solution of the Stommel–Munk equation on a polygon representing the Mediterranean Sea, demonstrates how the proposed method can be used in a real-world application.

3.1 Equations for wind-driven ocean circulation

In this section, the Stommel model and the Stommel–Munk model are first explained and then discretized using the meshfree collocation described in Chapter 2.

3.1.1 Linearized stationary quasi-geostrophic equations (SQGE)

As explained in Chapter 1, the quasi-geostrophic equations of the ocean are time-dependent and nonlinear. However, linearized, stationary versions of these equations are available. Examples of these linearized SQGE are the Stommel and Stommel–Munk models. While the Stommel model is a second-order PDE with respect to the streamfunction ψ, the Stommel–Munk model is a fourth-order PDE. Similar to the QGE, the Stommel–Munk model contains the biharmonic term $\Delta^2\psi$, the wind forcing term F, and the rotational term $\partial\psi/\partial x$ to include the effect of an asymmetry in the east-west direction. The Stommel–Munk model involves a Laplacian term $\Delta\psi$ instead of the nonlinear Jacobian term.

We consider a plane domain Ω with boundary Γ. The Stommel–Munk model [27] is given by

$$\begin{aligned} -\epsilon_{\mathrm{s}}\Delta\psi + \epsilon_{\mathrm{m}}\Delta^2\psi - \frac{\partial\psi}{\partial x} &= F \quad \text{in} \quad \Omega, \\ \psi = 0 \quad \text{and} \quad \nabla\psi\cdot\mathbf{n} &= 0 \quad \text{on} \quad \Gamma \end{aligned} \tag{3.1}$$

where $\mathbf{n}$ is the outward unit normal vector on the boundary Γ. For wind-driven ocean circulation in an enclosed mid-latitude basin, let ψ and F denote the velocity streamfunction and the wind forcing, respectively. The parameters ϵ_{s} and ϵ_{m} are the non-dimensional Stommel and Munk numbers, respectively, which are defined by

$$\epsilon_{\mathrm{s}} = \frac{\gamma}{\beta L} \quad \text{and} \quad \epsilon_{\mathrm{m}} = \frac{A}{\beta L^3}. \tag{3.2}$$

Here, γ is the coefficient of the linear drag (or the Rayleigh friction) as might be generated by a bottom Ekman layer, β is the coefficient multiplying the y-coordinate in the β-plane approximation, A is the eddy viscosity parametrization, and L is the characteristic length scale.

The Stommel model (Vallis [27]) is given by

$$\begin{aligned} -\epsilon_{\mathrm{s}}\Delta\psi - \frac{\partial\psi}{\partial x} &= F \quad \text{in} \quad \Omega, \\ \psi &= 0 \quad \text{on} \quad \Gamma \end{aligned} \tag{3.3}$$

where ϵ_{s} is the Stommel number defined in (3.2). Unlike the Stommel–Munk model, the Stommel model is a second-order PDE and only $\psi = 0$ is imposed on the boundary.

3.1.2 Discretization of governing equations

For convenience, we define $\Lambda = \Lambda_i \cup \Lambda_b$ where Λ_i is the set of N_{i} interior nodes and Λ_b is the set of N_{b} boundary nodes, with $N_{\mathrm{i}} + N_{\mathrm{b}} = N$ total nodes. If $\Phi_{IJ}^{\boldsymbol{\alpha}_k}$ is used to denote the Jth entry of the $\boldsymbol{\alpha}_k$th derivative operator at $\mathbf{x}_I$, then substituting (2.11) into (3.1) yields the discrete form of the Stommel–Munk PDE:

$$\sum_{J=1}^{N}\{-\epsilon_{\mathrm{s}}[\Phi_{IJ}^{(2,0)} + \Phi_{IJ}^{(0,2)}] + \epsilon_{\mathrm{m}}[\Phi_{IJ}^{(4,0)} + 2\Phi_{IJ}^{(2,2)} + \Phi_{IJ}^{(0,4)}] - \Phi_{IJ}^{(1,0)}\}\psi_J = F(\mathbf{x}_I) \tag{3.4}$$

for each $\mathbf{x}_I \in \Lambda_i$. The boundary conditions are similarly discretized as

$$\sum_{J=1}^{N}\Phi_{IJ}^{(0,0)}\psi_J = 0, \qquad \sum_{J=1}^{N}[\Phi_{IJ}^{(1,0)}n_1 + \Phi_{IJ}^{(0,1)}n_2]\psi_J = 0 \tag{3.5}$$

for each $\mathbf{x}_I \in \Lambda_b$. If we define $\mathbf{F}^{\mathrm{i}} \equiv \{F(\mathbf{x}_1), F(\mathbf{x}_2), ..., F(\mathbf{x}_{N_i})\}^{\mathrm{T}}$, then these discretized equations may be assembled into an $(N_i + 2N_b) \times N$ system

$$\mathbf{K}\boldsymbol{\psi} = \mathbf{F} \tag{3.6}$$

where

$$\mathbf{K} = \begin{bmatrix} \mathbf{K}^{\mathrm{i}} \\ \mathbf{K}^{\mathrm{d}} \\ \mathbf{K}^{\mathrm{n}} \end{bmatrix} \qquad \text{and} \qquad \mathbf{F} = \begin{bmatrix} \mathbf{F}^{\mathrm{i}} \\ \mathbf{0} \\ \mathbf{0} \end{bmatrix}. \tag{3.7}$$

In (3.7), the (I, J) entry of the $N_i \times N$ block K^{i} is given by

$$K_{IJ}^{\mathrm{int}} = -\epsilon_{\mathrm{s}}[\Phi_{IJ}^{(2,0)} + \Phi_{IJ}^{(0,2)}] + \epsilon_{\mathrm{m}}[\Phi_{IJ}^{(4,0)} + 2\Phi_{IJ}^{(2,2)} + \Phi_{IJ}^{(0,4)}] - \Phi_{IJ}^{(1,0)} \tag{3.8}$$

The (I, J) entry of the $N_b \times N$ block K^{d} is given by

$$K_{IJ}^{\mathrm{d}} = \Phi_{IJ}^{(0,0)} \tag{3.9}$$

Finally, the (I, J) entry of the $N_b \times N$ block K^{n} is given by

$$K_{IJ}^{\mathrm{n}} = \Phi_{IJ}^{(1,0)} n_1 + \Phi_{IJ}^{(0,1)} n_2 \tag{3.10}$$

Similarly, by substituting (2.11) into (3.3), the discrete form of the Stommel equation and its boundary conditions can be obtained as

$$\begin{gathered} \sum_{J=1}^{N} \{-\epsilon_{\mathrm{s}}[\Phi_{IJ}^{(2,0)} + \Phi_{IJ}^{(0,2)}] - \Phi_{IJ}^{(1,0)}\} \psi_J = F(\mathbf{x}_I), \quad \text{for } \mathbf{x}_I \in \Lambda_i \\ \text{and} \qquad \sum_{J=1}^{N} \Phi_{IJ}^{(0,0)} \psi_J = 0, \quad \text{for } \mathbf{x}_I \in \Lambda_d. \end{gathered} \tag{3.11}$$

These equations can also be assembled into a system like (3.6), this time $N \times N$, with

$$\mathbf{K} = \begin{bmatrix} \mathbf{K}^{\mathrm{i}} \\ \mathbf{K}^{\mathrm{d}} \end{bmatrix} \qquad \text{and} \qquad \mathbf{F} = \begin{bmatrix} \mathbf{F}^{\mathrm{i}} \\ \mathbf{0} \end{bmatrix}. \tag{3.12}$$

where the (I, J) entries of the $N_i \times N$ block K^{i} and the $N_b \times N$ block K^{d} are given by

$$K^{\mathrm{i}}_{IJ} = -\epsilon_{\mathrm{s}}[\Phi^{(2,0)}_{IJ} + \Phi^{(0,2)}_{IJ}] - \Phi^{(1,0)}_{IJ}, \quad K^{\mathrm{d}}_{IJ} = \Phi^{(0,0)}_{IJ}. \tag{3.13}$$

3.2 Numerical study

To verify our method, we perform numerical studies on three benchmark problems commonly used in geophysical fluid dynamics [27]. The first two problems involve the Stommel model on a rectangular domain with a strong western boundary layer and the Stommel–Munk model without a strong western boundary layer, presented in 3.2.1 and 3.2.2. The results from these studies motivate an examination of the effect of numerical parameters of the proposed method on error behavior in the context of these benchmark problems, presented in 3.2.3. After this investigation, results from the third benchmark problem, the Stommel–Munk equation on a rectangular domain with a strong western boundary layer, are discussed in 3.2.4. This includes results from applying a local refinement of the discretization. Finally, the proposed method is used to solve the Stommel–Munk equation on a polygonal domain representing the Mediterranean Sea in 3.2.5.

In the subsequent studies, we analyze convergence and error behavior by defining the the following discrete L^2-norm and L^∞-norm errors:

$$\|e\|_2 \equiv \sqrt{\frac{\Sigma_{i=1}^N (\psi_i^h - \psi_i)^2}{\Sigma_{i=1}^N (\psi_i)^2}} \tag{3.14}$$

and

$$\|e\|_\infty \equiv \frac{\max|\psi_i^h - \psi_i|}{\max|\psi_i|}, \tag{3.15}$$

respectively, where ψ^h is the approximation of the exact solution ψ. In (2.6), the weight function does not need to be differentiable. Hence, all simulations are performed using the

weight function

$$w\left(\frac{\mathbf{x}_I - \mathbf{y}}{\rho(\mathbf{y})}\right) = \left(1 - \left\|\frac{\mathbf{x}_I - \mathbf{y}}{\rho(\mathbf{y})}\right\|\right)^4. \tag{3.16}$$

The dilation parameter ρ, which represents the radius of the domain of influence of each collocation point, should be chosen so that the resulting differential operators are sparse to save computational cost. On the other hand, ρ should be large enough so that the $\mathbf{M}$ matrices are nonsingular and the solution is accurate. In general, there is some minimum number of points in a domain of influence such that all $\mathbf{M}$ matrices (2.8) are nonsingular [14]. This number of points dictates the radius of influence of each collocation point based on the spacing of nodes and the geometry of the domain. More discussion of the dilation parameter related to a specific example can be found in Section 3.2.3.

3.2.1 Stommel model

We consider the test problem (3.3) with the exact solution

$$\psi(x,y) = \frac{\sin(\pi y)}{\pi(1+4\pi^2\epsilon_{\mathrm{s}}^2)}\left[2\pi\epsilon_{\mathrm{s}}\sin(\pi x) + \cos(\pi x) + \frac{(1+e^{R_2})e^{R_1 x} - (1+e^{R_1})e^{R_2 x}}{e^{R_1} - e^{R_2}}\right] \tag{3.17}$$

over the domain $\Omega = [0,1]\times[0,1]$, where R_1 and R_2 are given by

$$R_1 = \frac{-1+\sqrt{1+4\pi^2\epsilon_{\mathrm{s}}^2}}{2\epsilon_{\mathrm{s}}} \qquad \text{and} \qquad R_2 = \frac{-1-\sqrt{1+4\pi^2\epsilon_{\mathrm{s}}^2}}{2\epsilon_{\mathrm{s}}}. \tag{3.18}$$

This example was used for the test of an algorithm by Myers and Weaver [32], Foster et al. [35], and Kim et al. [39]. Upon taking $\epsilon_{\mathrm{s}} = 0.05$, we work in a setting identical to that considered in these references. The forcing term F is chosen to match with that given by the exact solution (3.17). As shown in Figures 3.1 and 3.2, a rectangular ocean is chosen as a computational domain. With the origin of a Cartesian coordinate system at the southwest corner, the x- and y-axis point eastward and northward, respectively, and the boundaries of the computational domain are the shores of the ocean.

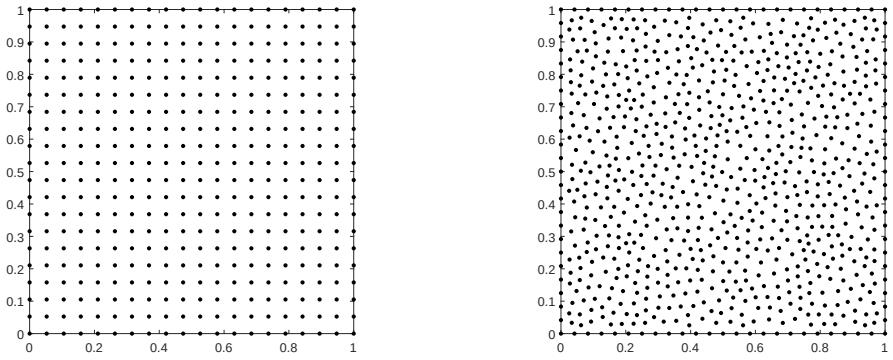

Figure 3.1: Examples of (a) a uniform distribution of 400 collocation points and (b) a random distribution of 821 collocation points

In Figure 3.1, we display uniform and random distributions of collocation points used for this study. In Figure 3.2, we compare the streamlines of the numerical solution using the randomly distributed collocation points with the exact solution. Both solutions are qualitatively indistinguishable from the exact solution. Notice that the similar solution using the uniform distribution of collocation points is observed.

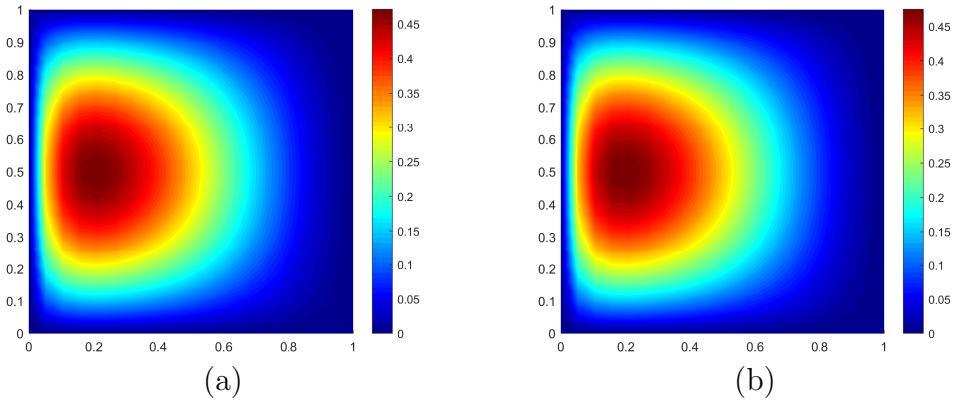

Figure 3.2: Contour plot of the streamfunction for the Stommel model: (a) the numerical solution and (b) the exact solution given by (3.17)

To study convergence rates as a function of average nodal distance h, $\|e\|_2$ and $\|e\|_\infty$ are measured for approximately $h = \{0.020, 0.017, 0.014, 0.012\}$. Our method and the finite-difference method (FDM) both use a Taylor expansion to approximate a solution variable.

Table 3.1: Convergence rates in L^2-norm $\|e\|_2$ and L^∞-norm $\|e\|_\infty$ with a second-order polynomial using uniform distributions of collocation points

# of collocation points	$\|e\|_2$	$\|e\|_\infty$
2500	5.20e-03	1.27e-02
3600	3.38e-03	7.86e-03
4900	2.36e-03	5.21e-03
6400	1.73e-03	3.63e-03
Convergence rate	2.31	2.61

Table 3.2: Convergence rates in $\|e\|_2$ and $\|e\|_\infty$ with a second-order polynomial using random distributions of collocation points

# of collocation points	$\|e\|_2$	$\|e\|_\infty$
2212	7.16e-03	2.24e-02
3297	4.52e-03	1.31e-02
4705	2.92e-03	7.57e-03
6465	2.02e-03	5.03e-03
Convergence rate	2.37	2.82

Thus, based on such a similarity with the FDM, we expect that our approach also has an optimal order of convergence equal to the order of the Taylor expansion used. In other words, the optimal convergence rates for our method would be quadratic or quartic for the second-order and fourth-order polynomials, respectively. Theoretical study for the error analysis of the proposed method remains as the authors' future work. Some theoretical work for similar types of strong form meshfree methods can be found in [14, 25]. For the second-order polynomial, Table 2 and Table 3 show the convergence rates for uniformly and randomly distributed collocation points in both L^2- and L^∞-norm errors. The plots of convergence rate in L^2-norm for both second-order and fourth-order polynomials are displayed in Figure 3.3 and Figure 3.4. Note that the presented convergence analysis results, such as Fig. 3.3, adopted log-log plots, although it is sometimes hard to recognize this due to the small range of values on the horizontal axis.

In Table 3.3, we summarize the convergence rates for the second-order and fourth-order polynomials for the Stommel model with the exact solution given by (3.17). The results show higher than the expected convergence rates in both L^2-norm and L^∞-norm.

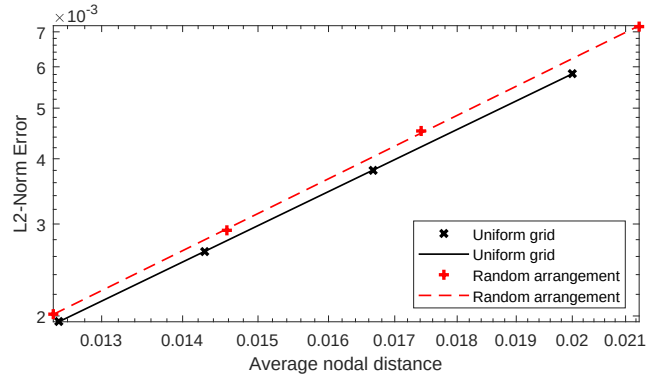

Figure 3.3: Convergence plot in $\|e\|_2$ for the Stommel model using the 2nd-order polynomial approximation. Slopes of the regression lines: 2.31 (uniform) and 2.37 (random)

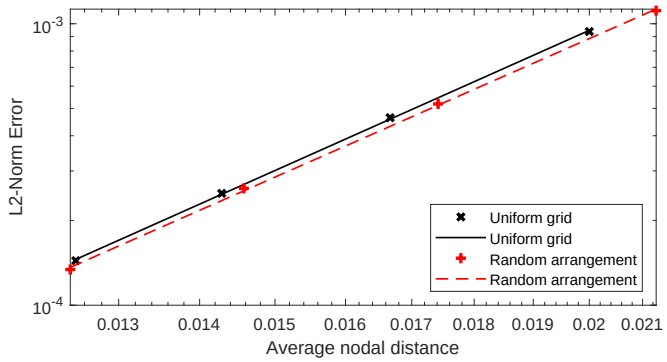

Figure 3.4: Convergence plot in $\|e\|_2$ for the Stommel model using the 4th-order polynomial approximation. Slopes of the regression lines: 4.11 (uniform) and 4.16 (random)

3.2.2 The Stommel–Munk model without western boundary layer

In contrast to the Stommel model, a challenge in solving the fourth-order Stommel–Munk model is the need to apply two Dirichlet boundary conditions $\psi = \nabla\psi \cdot \mathbf{n} = 0$ on the entire boundary. In applying the proposed method to a second-order PDE with only one boundary condition, nodal solutions are found by solving a linear system in which each equation is a discretized version of (3.1) (for each of N_i interior collocation points) or of the boundary condition (for N_b boundary nodes). In this way, boundary conditions are applied directly, and the resulting system of equations is square. However, for the Stommel–Munk model, to apply both boundary conditions at each boundary node, two separate equations must be written for each boundary node as shown in (3.5). This leads to a total of $N_\mathrm{i}+2N_\mathrm{b}$ equations

Table 3.3: Convergence rates in $\|e\|_2$ and $\|e\|_\infty$ with a second-order polynomial using random distributions of collocation points

Nodal arr.	2nd order		4th order	
	$\|e\|_2$	$\|e\|_\infty$	$\|e\|_2$	$\|e\|_\infty$
Uniform grid	2.31	2.61	4.11	3.99
Random	2.37	2.82	4.16	4.07

in $N_\mathrm{i} + N_\mathrm{b}$ unknown nodal values of ψ, i.e., an overdetermined system of equations.

Our approach is to solve this overdetermined system by the method of weighted least squares. Introducing a diagonal matrix $\mathbf{D}$ containing positive weight values along its diagonal into the system of equations (3.6), the solution $\boldsymbol{\psi}$ that minimizes the norm $(\mathbf{K}\boldsymbol{\psi} - \mathbf{F})^T\mathbf{D}^2(\mathbf{K}\boldsymbol{\psi} - \mathbf{F})$ is obtained by solving

$$\mathbf{K}^T\mathbf{D}^2\mathbf{K}\boldsymbol{\psi} = \mathbf{K}^T\mathbf{D}^2\mathbf{F}. \tag{3.19}$$

Why might it be advantageous to use some weight values in $\mathbf{D}$ other than 1.0 (standard least squares)? As an example, consider a problem in which the error between the numerical solution and the analytical solution is highest at the boundary when standard least squares is used. Then, increasing the weight values applied to the boundary condition equations penalizes this higher error at the boundary more heavily than does standard least squares, potentially resulting in lower maximum or L^2-error of the numerical solution. A discussion of how weights are chosen for the problems in this study may be found in Section 3.2.3.

Using this weighted least squares strategy, we test the Stommel–Munk model on a rectangular ocean in similar fashion to the Stommel model. We consider a benchmark example that is commonly used to test a finite-element algorithm [33, 39]. This example has a forcing F corresponding to the exact solution given by

$$\psi(x, y) = \sin^2(\pi x/3)\sin^2(\pi y) \quad \text{in } \Omega = [0, 3] \times [0, 1]. \tag{3.20}$$

The Stommel and Munk numbers are chosen to be $\epsilon_\mathrm{s} = 0.05$ and $\epsilon_\mathrm{m} = 6.0\times10^{-5}$, respectively.

To approximate the fourth-order derivative operators, at least a fourth-order polynomial is required. As a result, we use fourth-order polynomials in this study. When assembling the overdetermined system of equations in the solution of this problem, weights of 1.0 are chosen for the rows corresponding to interior collocation points, whereas weights of 0.2 are used for the rows corresponding to boundary points. A more thorough discussion of this choice of relative weights may be found in Section 3.2.3.

In Figure 3.5, we display the streamlines of both numerical and exact solutions for the fourth-order polynomial. Both results are qualitatively indistinguishable. In Figure 3.6, the rates of convergence in L^2-norm for both uniform and random distributions of collocation points are presented. Moreover, convergence rates in both L^2 and L^∞-norms are summarized in Table 3.4. While the order of convergence in L^2-norm is quartic, slightly lower convergence rate is observed in L^∞-norm.

Table 3.4: Convergence rates in $\|e\|_2$ and $\|e\|_\infty$ with a fourth-order polynomial using uniform and random distributions of collocation points for the test problem with the exact solution (3.20)

Nodal arr.	$\|e\|_2$	$\|e\|_\infty$
Uniform grid	4.20	3.87
Random	4.06	3.74

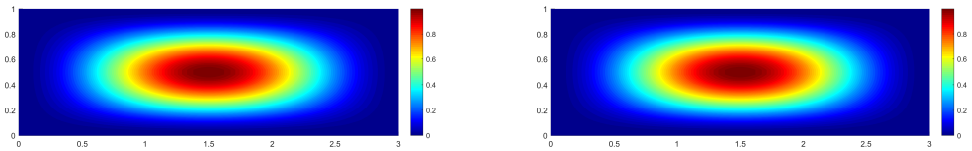

(a) (b)

Figure 3.5: Comparison between (a) numerical and (b) exact solutions of the Stommel–Munk model for the test problem with the exact solution (3.20)

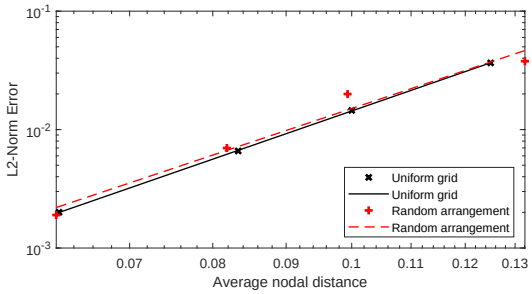

Figure 3.6: Convergence in $\|e\|_2$ for the 4th-order polynomial approximation for the problem with the exact solution given by (3.20). The slopes of the regression lines are 4.20 (uniform) and 4.06 (random)

3.2.3 Study of error behavior for numerical parameters

While obtaining results for the Stommel–Munk model above with the exact solution given by (3.20), it became apparent that the error behavior of the numerical solution is sensitive to the least squares weight values chosen for the diagonal matrix $\mathbf{D}$ in (3.19) and the number of neighbors chosen for the compact support of each collocation point. This section explores the effect of these numerical parameters on error behavior of the proposed collocation method.

First, we conduct a numerical experiment to determine the effect of weight values on the error behavior. The Stommel–Munk model with the exact solution (3.20) is used as a basis for this study. The number of neighbors in the compact support is held fixed at 35. Weights corresponding to the interior nodes are fixed at 1.0, while weights corresponding to the boundary nodes are varied between 0.001 and 100. We study the order of convergence in both L^2-norm and L^∞-norm for both the uniform grid and random arrangements. The order of convergence is based on the following ranges of total numbers of collocation points: For the uniform grid, error is computed for 243, 300, 432, and 675 total points; for the random arrangement, error is computed for 172, 304, 448, and 775 total points. In addition to convergence rates, the values of $\|e\|_2$ and $\|e\|_\infty$ are recorded for a fixed number of collocation points (675 in the uniform grid case and 775 in the random arrangement case). The results are displayed in Figure 3.7 and Figure 3.8.

For the uniform grid, the highest rate of convergence appears to occur when the boundary

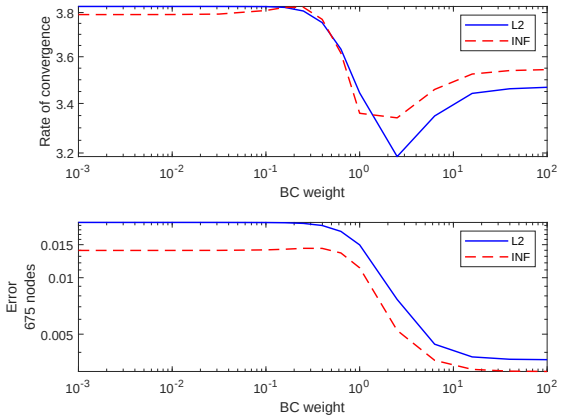

Figure 3.7: Effect of BC weights on error behavior, uniform grid

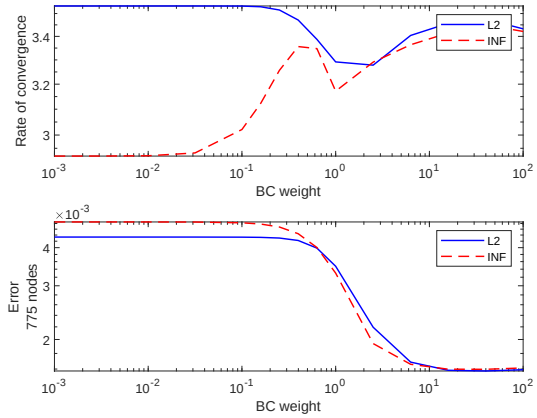

Figure 3.8: Effect of BC weights on error behavior, random arrangement

condition (BC) weights are less than 1.0, but this choice produces largest overall error of the solution for a fixed number of collocation points. A possible explanation for this phenomenon is the following: When BC weights are less than 1.0, the error tends to be high at the boundary and the weighted least squares method penalizes this high boundary error very little. As a consequence, for low BC weights, the overall spatial distribution of error is unbalanced with highest error at the boundary, causing the L^2-norm $\|e\|_2$ and L^∞-norm $\|e\|_\infty$ errors to be relatively high. However, increasing the density of the collocation points causes this boundary error to disappear rapidly, resulting in a high rate of convergence. Conversely, strictly penalizing boundary error with larger weight values results in lower overall error even for coarse discretizations, resulting in a lower rate of convergence. The

spatial distributions of error for two BC weight values, shown in Figure 3.9, bear out this hypothesis. It is noteworthy that a choice of weights around 1.0 to 3.0 results in high error and in the lowest rates of convergence, suggesting that it can indeed be advantageous to vary weight values away from 1.0 for the boundary condition equations. Further research should investigate what characteristics of a problem (e.g., the forcing term) make it advantageous or disadvantageous to do so.

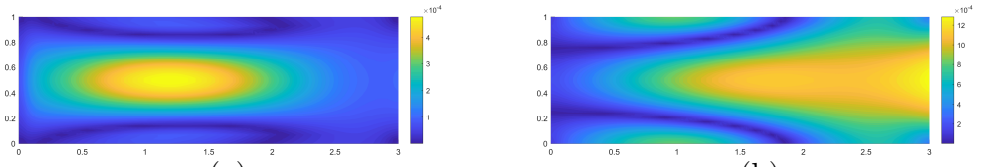

(a) (b)

Figure 3.9: Spatial distribution of absolute error for (a) BC weight = 5.0 and (b) BC weight = 0.2

Similar error behavior occurs in the case of the random nodal arrangement, except with respect to the rate of convergence in the L^2-norm $\|e\|_2$ compared to the L^∞-norm $\|e\|_\infty$ errors for small values of BC weights. In this case, it is possible that the maximum value of the error is localized to a few isolated collocation points at the boundary, which would cause the maximum error to decrease slowly compared to the L^2-norm error as the density of the collocation points is increased. It is worth noting that the level of discretization and the boundary condition weights (i.e. the matrix D) both have a limited effect on the condition number of the matrix $\mathbf{K}^T\mathbf{D}^2\mathbf{K}$ in Eq. (3.19). However, proposed method has not exhibited a severe dependency on the condition numbers according to the authors' experience.

We also conducted a numerical experiment to determine the effect on error behavior of the number of neighbors chosen for the compact support of each collocation point. As before, the problem with the exact solution given by (3.20) was used. The weights applied to the interior node equations were again fixed at 1.0, but this time the BC weights were fixed at 0.5 for all boundary nodes. The number of neighbors specified for the compact support of each collocation point was varied between 30 and 50. In each trial, the dilation

parameter at each collocation point was taken to be the distance between the collocation point and the farthest of its 30-50 neighbors identified using the k-nearest neighbors (KNN) search algorithm [60]. An alternative algorithm to construct spatially varying continuous compact support function, which uses a pseudo-counting function constructed based on collocation point density, is described in [61]. Again, the convergence rates and error values were measured for each choice of number of neighbors, for a uniform grid of points. The results are shown in Figure 3.10.

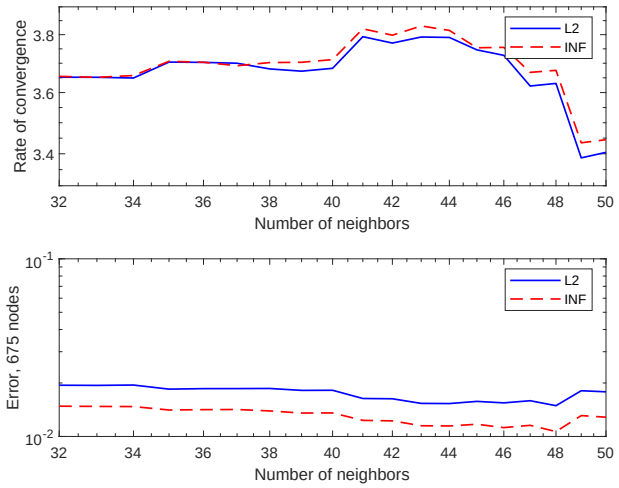

Figure 3.10: Effect of the number of neighbors in compact support on error behavior, uniform grid

The highest rates of convergence were achieved when 41–43 neighbors were used. Some of the lowest values of error for a fixed number of nodes were also achieved for this range of numbers of neighbors. These results suggest that, for a uniform grid of collocation points, there is an optimal number of neighbors to specify for the compact support. We propose the following reason for the sensitivity of the error behavior to this parameter: Depending on the number of neighbors chosen, the spatial pattern of neighbor nodes in a compact support will be one of a variety of shapes. Thus, just as the error behavior of the FDM depends on the choice of a five-point stencil versus a nine-point stencil due to the relative positions of the neighbors and their effect on the numerical solution, so too is the present method sensitive

to the choice of spatial pattern of neighborhood nodes.

Based on the studies discussed in this section, values of number of neighbor nodes and BC weights were chosen so as to optimize the convergence rate for the above problem, leading to the results displayed in Table 3.4 from the previous section.

3.2.4 Stommel–Munk model with western boundary layer

Having studied the effect of numerical parameters on error behavior, we are able to use our method to solve the Stommel–Munk model with a different forcing term. This problem has a forcing corresponding to the exact solution given by

$$\psi(x,y) = \left[(1-x/3)(1-e^{-20x})\sin(\pi y)\right]^2. \tag{3.21}$$

In contrast to the previous example in Section 3.2, this one has a strong western boundary layer as shown in Figure 3.11. This boundary layer results in a region of very high gradient on the left side of the domain, which is difficult to capture. For this reason, fourth- and fifth-order polynomials are unable to achieve reliable solutions due to instability on the left side of the domain. Thus, a sixth-order polynomial is used. Fortunately, the jump in computational cost due to using a sixth-order polynomial approximation rather than a fourth-order approximation is relatively small because the number of small matrices needing to be inverted while computing the differential operators remains unchanged.

A comparison of the numerical solution with the exact solution shows qualitative agreement, as shown in Figure 3.11. Moreover, as shown in Table 3.5, for the uniform grid arrangement of collocation points, slightly lower than optimal (sixth-order) convergence rate is obtained in both $\|e\|_2$ and $\|e\|_\infty$ due to the presence of the western boundary layer. The convergence for uniform collocation points is remarkably steady, as shown in Figure 3.12. For the random arrangement of collocation points, low convergence rates and largely unpredictable error behavior are observed due to local instabilities in the solution.

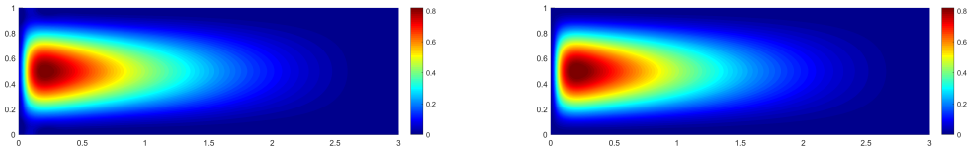

(a) (b)

Figure 3.11: Comparison between (a) numerical and (b) exact solutions of the Stommel–Munk model with the western boundary layer

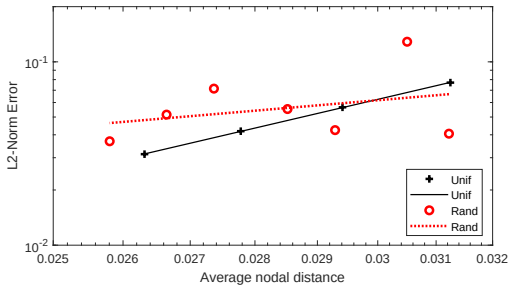

Figure 3.12: Convergence in $\|e\|_2$ for the Stommel–Munk model with the western boundary layer

To improve accuracy, local refinement is applied to the left side of the domain where the strong western boundary layer is found. This is done for both uniform and random arrangements of collocation points. For the uniform grid, we locally refined the domain by placing an extra collocation point at the centroid of each group of four existing nodes in the left sixth of the domain. For the random arrangement, the left sixth of the domain had an average nodal distance three times that of the right side of the domain; the `gmsh` software allowed a smoother transition between the right side of the domain and the locally refined area on the left than in the case of the uniform grid. Examples of the refined nodal arrangements used are given in Figure 3.14.

Figure 3.13 shows the convergence plots in $\|e\|_2$ for uniform and random arrangements with and without local refinement. Table 3.5 contains the rates of convergence for these various schemes in $\|e\|_2$ and $\|e\|_\infty$. It should be noted that in the case of both uniform and random arrangements, the rate of convergence for the refined nodal arrangements is much

better than that for the uniform-density nodal arrangements. In addition, the errors for the refined random arrangement are the lowest of all the schemes, suggesting that properly implemented refinement would improve both the accuracy and the rate of convergence of the numerical solution for a problem with a high-gradient region such as this one.

As shown in Fig. 3.13, instability (or suboptimal convergence) is exhibited by the proposed method for the western boundary layer example, especially for the random arrangements of collocation points. As explained in [25], this is expected since the proposed method's formulation is based on the strong form and avoids the Galerkin framework. Currently, to the best of the authors' knowledge, there are no theoretical stability and perturbation analyses available for the proposed method other than numerical studies of the method. More numerical results for the discretization sensitivity-induced instability of the method within similar contexts can be found in authors' previous works [24, 21, 19]. Theoretical study for the error and stability analysis of the proposed method remains part of the authors' future work.

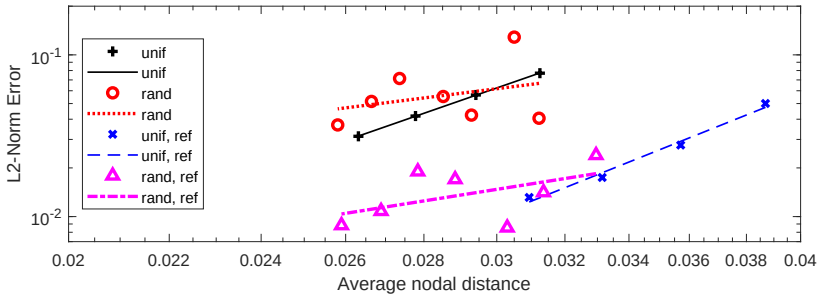

Figure 3.13: Influence of local refinement for the Stommel–Munk model with the western boundary layer

3.2.5 Wind-driven ocean circulation in the Mediterranean Sea

To demonstrate the usefulness of the proposed method in solving real-world problems on arbitrary shaped domains, the method is used to solve the Stommel–Munk model on the

Table 3.5: Rate of convergence (ROC) in $\|e\|_2$ and $\|e\|_\infty$ with local refinement for both uniform and random distributed collocation points

Scheme	ROC in $\|e\|_2$	ROC in $\|e\|_\infty$
Unif.	5.23	5.78
Rand.	1.90	1.27
Unif. ref.	6.02	7.65
Rand. ref.	2.39	2.81

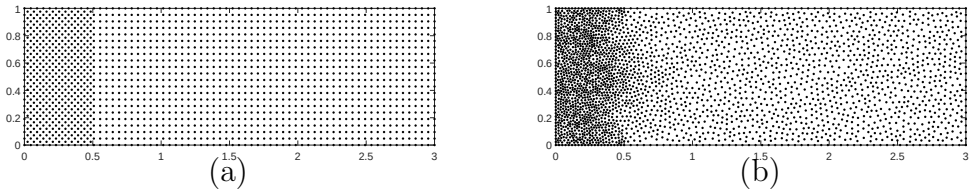

Figure 3.14: Illustration of nodal arrangements for local refinement applied to (a) uniformly spaced collocation points and (b) randomly spaced collocation points

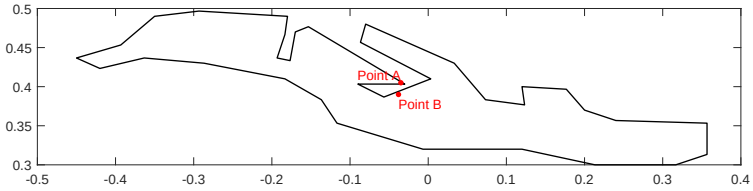

Figure 3.15: Polygon representing the boundary of the Mediterranean Sea

interior of a polygon representing the coastlines of the Mediterranean sea. This example was studied by Foster et al. [35] and Jiang and Kim [41] for the test of their finite-element formulations of the stationary quasi-geostrophic equations. We use the forcing term $F = \sin(\pi y/4)$ arising from the derivative of the wind stress (Myers and Weaver [32]). The same values of the Stommel and Munk numbers (0.05 and 6.0×10^{-5}, respectively) are used. Notice that an analytical solution is not available, so a convergence study cannot be performed.

This polygon shown in Figure 3.15 encloses a simply connected region. However, this region's concavity and various narrow subregions present challenges to solving the model on its interior. The first challenge in solving the Stommel-Munk model on this domain is that of

generating an arrangement of collocation points for the Mediterranean sea region. Without an unreasonable degree of refinement, the use of a uniform tensor-product grid of points would have been insufficient to capture the geometry of the region. Even in the case of the rectangular domain with western boundary layer in Section 3.2.4, the random arrangement with selective refinement resulted in consistently lower error than the uniform grid with no refinement, as shown in Fig. 3.13. The random arrangement was also less cumbersome to produce than the uniform grid with selective refinement. For domains with complicated geometry, producing a uniform grid with selective refinement is much more difficult and tedious, while producing a random arrangement with selective refinement remains straightforward using readily available FEM meshing software. Thus, for complicated geometries, a selectively refined random arrangement of collocation points is more practical than a selectively refined uniform arrangement, but still exhibits less error for a given number of collocation points than a uniform grid with no selective refinement. Thus, generating a random arrangement of nodes is preferred and left to the open-source meshing software `gmsh` [62]. Each segment of the polygon boundary is assigned a number of boundary collocation points approximately proportional to this segment's fraction of the total length of the boundary. If this results in a number of boundary nodes that is too small for this segment (e.g., only two or three nodes), this segment is assigned five nodes. Given these specifications, `gmsh` generated the arrangement of collocation points shown in Figure 3.16.

After discretizing the region, another challenge is to ensure that the domain of influence of each collocation point is reasonable despite the concavity of some parts of the domain. For example, consider points A and B in Figure 3.15. Although these points are very close each other, the solution of the PDE at point A cannot reasonably be expected to affect the solution at point B because these points are separated by land. Thus, the domain of influence of point A should exclude point B and vice-versa. To accomplish such exclusions, the domain is divided into the subregions as shown in Figure 3.17. Then, in selecting the points to include in the domain of influence of a given point D, only candidate points from

the subregion containing point D or adjacent subregions are considered.

Using MATLAB's `knnsearch` accomplishes this task of selecting points for the domain of influence of each point. Each domain of influence contains 18 collocation points, which proved the optimal number of points in terms of ensuring invertibility of the **M** matrix (2.8), stability of the solution field at the boundary, and reasonable computational time. Finally, the value chosen for the dilation parameter ρ at each collocation point D was simply the distance between point D and the farthest-away point in the domain of influence of point D. An illustration of the domain of influence for a point in this problem and related ideas is shown in Figure 3.18. Once these tasks are complete, we solve the Stommel–Munk

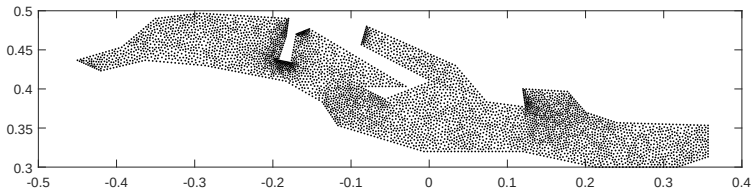

Figure 3.16: Arrangement of 4,834 collocation points used for the Mediterranean sea example

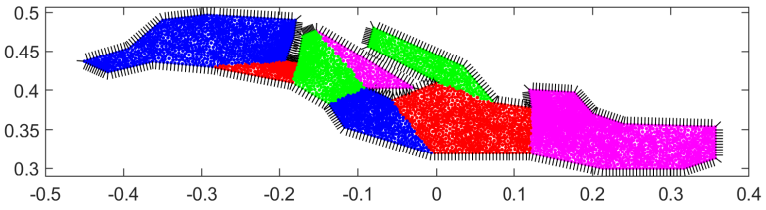

Figure 3.17: Mediterranean Sea domain subdivided into cells in order to control the domain of influence of each collocation point and direction of the normal vectors along the boundary

model using the point collocation method. In order to balance the errors between the boundary and the interior, we choose BC weights corresponding to the boundary condition $\mathbf{u} = 0$ as 100 times those corresponding to the zero-flux boundary condition $\nabla\mathbf{u} \cdot \mathbf{n} = 0$. A similar scheme weighting the Dirichlet boundary condition equations more heavily than

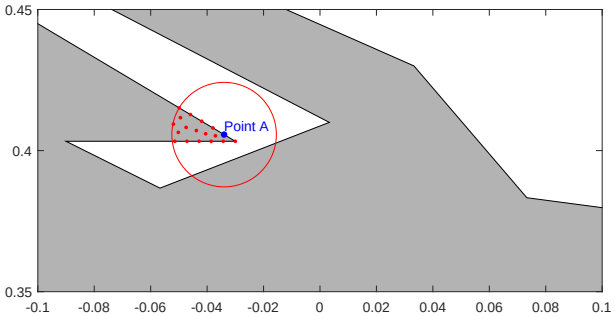

Figure 3.18: Domain of influence of Point A (largest dot, in blue) from Figure 3.15 containing 18 points. The radius of the circle is ρ for Point A. Note that the domain of influence does not contain points from the subregion across land from Point A

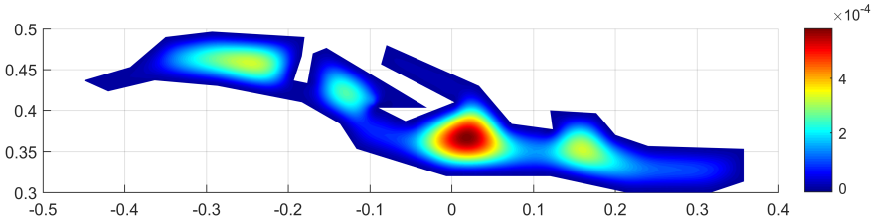

Figure 3.19: Contour plot of the numerical solution in the Mediterranean Sea example

the Neumann boundary condition equations was used in the weighted collocation method of Chen et al. [63]; one should refer to the guidelines presented in [63] to choose the proper values of BC weights for a general problem. In Figure 3.19, we display a contour plot of the streamfunction. The plot shows qualitative agreement with the one obtained using finite-element methods by Foster et al. [35] and Jiang and Kim [41]. This result verifies the capability of our method on realistic ocean circulation problems with arbitrary shaped coastal boundaries.

Chapter 4

Thermomechanical Contact

The next test of the proposed method is whether it can be used to solve nonlinear PDEs. The problem of multi-body thermomechanical contact provides such nonlinear PDEs. Section 4.1 details the formulation of these equations. Section 4.2 describes how these equations are discretized using the differential operators formulated in 2. Finally, Section 4.3 examines three numerical verification examples: frictional contact on an inclined surface, Hertzian contact between two half-cylinders, and thermomechanical contact between two rectangular blocks.

4.1 Equations for thermomechanical contact

In this section, the governing equations for thermomechanical contact are developed. First, an overview of the geometry, domain interior equations, and boundary conditions are given. Next, the mechanical contact constraints are described and regularized using a penalty approach. Finally, the thermal contact model is introduced.

4.1.1 Geometry, governing equations, and boundary conditions

This study concerns loosely coupled thermo-mechanical contact between two deformable bodies in two dimensions, the interiors of which are denoted by Ω^1 and Ω^2, as shown in Figure 4.1. For $\alpha \in \{1, 2\}$, the closure of the domain Ω^α is denoted by $\bar{\Omega}^\alpha$, i.e., $\bar{\Omega}^\alpha = \Omega^\alpha \cup \Gamma^\alpha$, where Γ^α is the entire boundary of the domain Ω^α. Each total boundary Γ^α is partitioned such that $\Gamma^\alpha = \Gamma^\alpha_u \cup \Gamma^\alpha_t \cup \Gamma^\alpha_c$ with $\Gamma^\alpha_u \cap \Gamma^\alpha_t = \Gamma^\alpha_u \cap \Gamma^\alpha_c = \Gamma^\alpha_c \cap \Gamma^\alpha_t = \emptyset$. Here, Γ^α_u denotes the subset of the boundary of Ω^α on which displacement $\mathbf{u}$ is prescribed, Γ^α_t the subset on which traction is prescribed, and Γ^α_c the subset on which contact between the two bodies is expected to occur. Each total boundary Γ^α is simultaneously partitioned in terms of temperature-related boundary conditions such that $\Gamma^\alpha = \Gamma^\alpha_\theta \cup \Gamma^\alpha_q \cup \Gamma^\alpha_c$ with $\Gamma^\alpha_\theta \cap \Gamma^\alpha_q = \Gamma^\alpha_\theta \cap \Gamma^\alpha_c = \Gamma^\alpha_c \cap \Gamma^\alpha_q = \emptyset$. Here, Γ^α_θ denotes the subset of the boundary of Ω^α on which temperature θ is prescribed and Γ^α_q the subset on which normal heat flux is prescribed. Finally, $\bar{\Omega} = \bar{\Omega}^1 \cup \bar{\Omega}^2$ is used to denote the entire domain of interest, namely the set of all points in either of the two bodies or their boundaries; $\Omega = \Omega^1 \cup \Omega^2$ denotes the interior thereof.

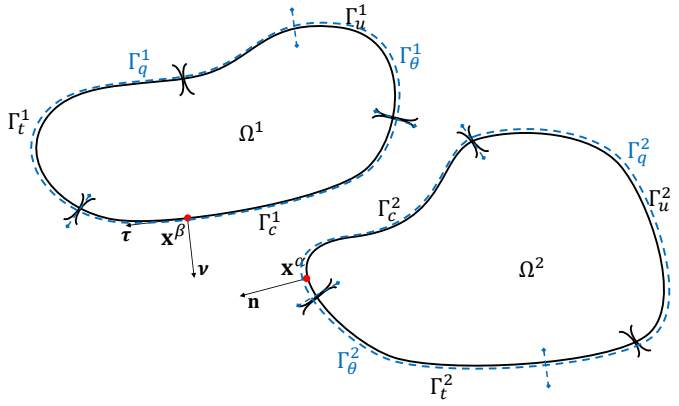

Figure 4.1: Notation for two-body contact

The objective in this study is to find the displacement $\mathbf{u}$ and change in temperature θ (from some reference temperature θ_0) over Ω that satisfy mechanical equilibrium and thermal equilibrium subject to boundary conditions. The equations for mechanical equilibrium are

given by

$$\nabla \cdot \boldsymbol{\sigma} + \mathbf{b} = 0 \quad \text{in } \Omega \tag{4.1}$$

Here, $\boldsymbol{\sigma}$ is the Cauchy stress tensor and $\mathbf{b}$ is a body force. Although the two bodies are permitted to have different material properties, they are assumed to be homogeneous, linear thermoelastic and isotropic. Thus, the appropriate constitutive equation is

$$\boldsymbol{\sigma} = 2\mu \left(\boldsymbol{\epsilon} - \boldsymbol{\epsilon}^{\theta}\right) + \lambda \text{tr} \left(\boldsymbol{\epsilon} - \boldsymbol{\epsilon}^{\theta}\right) \mathbf{1} \tag{4.2}$$

In (4.2), λ and μ are Lamé constants, $\mathbf{1}$ is the second-order identity tensor, and $\boldsymbol{\epsilon}$ is the mechanical strain tensor, and $\boldsymbol{\epsilon}^{\theta}$ is the thermal strain tensor. Small displacement and strain are assumed, so the mechanical strain is defined by

$$\boldsymbol{\epsilon} = \frac{1}{2} \left(\nabla \mathbf{u} + (\nabla \mathbf{u})^{\top}\right) \tag{4.3}$$

The thermal strain is related to the temperature change by

$$\boldsymbol{\epsilon}^{\theta} = \alpha_v \theta \mathbf{1} \tag{4.4}$$

The constant α_v in (4.4) is the coefficient of thermal expansion.

The equations for thermal equilibrium are given by

$$\nabla \cdot \mathbf{q} + s = 0 \tag{4.5}$$

Here, $\mathbf{q}$ is heat flux and s is a heat source. The heat flux is assumed to be proportional to the temperature gradient according to Fourier's Law:

$$\mathbf{q} = -\kappa \nabla \theta \tag{4.6}$$

The constant κ in (4.6) is the thermal conductivity.

Which fields $\mathbf{u}$ and θ satisfy the equations above depends on the boundary conditions. The field $\mathbf{u}$ at each point on the boundary Γ is subject to one (or a mix) of the following conditions:

$$\begin{aligned} \mathbf{u} &= \bar{\mathbf{u}} \quad \text{on } \Gamma_u^\alpha, \\ \boldsymbol{\sigma}\mathbf{n} &= \bar{\mathbf{t}} \quad \text{on } \Gamma_t^\alpha, \\ \boldsymbol{\sigma}\mathbf{n} &= \mathbf{t}^c \quad \text{on } \Gamma_c^\alpha \end{aligned} \tag{4.7}$$

for each $\alpha \in \{1, 2\}$. In (4.7), $\mathbf{n}$ is the unit outward normal vector to Ω, $\bar{\mathbf{u}}$ is the prescribed displacement on Γ_u^α, $\bar{\mathbf{t}}$ is the prescribed traction on Γ_t^α, and $\mathbf{t}^c$ is the contact pressure on Γ_c^α. This contact pressure is determined based on the formulation in subsequent sections. The field θ at each point on the boundary is subject to one of the following conditions:

$$\begin{aligned} \theta &= \bar{\theta} \quad \text{on } \Gamma_\theta^\alpha, \\ \mathbf{q}\cdot\mathbf{n} &= \bar{q} \quad \text{on } \Gamma_q^\alpha, \\ \mathbf{q}\cdot\mathbf{n} &= q^c \quad \text{on } \Gamma_c^\alpha \end{aligned} \tag{4.8}$$

In (4.8), $\bar{\theta}$ is the prescribed temperature change on Γ_θ^α, $\bar{q}$ is the prescribed normal heat flux on Γ_t^α, and q^c is the normal heat flux across the contact surface Γ_c^α.

The following sections describe the contact constraints that govern the interaction between $\bar{\Omega}^1$ and $\bar{\Omega}^2$. Some basic assumptions motivate the formulation presented here. First, at this length scale, it is assumed that there is no interpenetration between the two bodies during contact (although this assumption is relaxed during the penalty regularization of the normal contact constraint). Second, it is assumed that any force exerted on one body by the other is compressive, i.e., no cohesion exists between the bodies. Coulomb friction is assumed between the bodies, controlled by a coefficient of friction μ_f. Finally, it is assumed that the heat flux across the contact interface is strictly conductive and depends on the

contact pressure at the interface.

4.1.2 Normal and frictional contact constraints

First, we must define quantities associated with two points potentially in contact. Since both bodies subject to contact are deformable, the contact traction at a point $\mathbf{x}^\alpha \in \Gamma_c^\alpha$ will depend on the relative displacement between $\mathbf{x}^\alpha$ and the corresponding point $\mathbf{x}^\beta(\mathbf{x}^\alpha) \in \Gamma_c^\beta$ with which $\mathbf{x}^\alpha$ is potentially in contact. For each pair of corresponding contact points, a vector $\mathbf{n}(\mathbf{x}^\alpha)$ is used to denote the outward unit normal to Γ_c^α at $\mathbf{x}^\alpha$, while $\boldsymbol{\nu}(\mathbf{x}^\alpha) = \mathbf{n}(\mathbf{x}^\beta)$ is used to denote the outward unit normal to Γ_c^β at $\mathbf{x}^\beta$. The vector $\boldsymbol{\tau}(\mathbf{x}^\beta)$ denotes the unit tangent to Γ_c^β at $\mathbf{x}^\beta$. Specifically, this unit tangent is defined by

$$\boldsymbol{\tau} = \boldsymbol{\nu} \times \mathbf{e}_3 \tag{4.9}$$

where $\mathbf{e}_3$ is the unit basis vector pointing out of the paper. It is convenient to decompose the contact traction $\mathbf{t}^c$ at a point $\mathbf{x}$ into components along $\boldsymbol{\nu}$ and $\boldsymbol{\tau}$, as follows:

$$\mathbf{t}^c = \mathbf{t}_N - \mathbf{t}_T = t_N \boldsymbol{\nu} - t_T \boldsymbol{\tau} \tag{4.10}$$

For a more detailed discussion of these definitions, the reader is referred to Laursen's book [64].

Next, given a displacement field $\mathbf{u} : \Gamma_c^1 \cup \Gamma_c^2 \to \mathbb{R}^2$, we define a so-called gap function $g : \Gamma_c^1 \cup \Gamma_c^2 \to \mathbb{R}$ in terms of the relative displacement between a point on Γ^α and the corresponding contact point on Γ^β. Roughly speaking, the gap function represents the component of the vector between corresponding contact points in the deformed configuration normal to one of the contact surfaces. For all $\mathbf{x}^\alpha \in \Gamma_c^\alpha$ and $\mathbf{x}^\beta(\mathbf{x}^\alpha) \in \Gamma_c^\beta$,

$$g(\mathbf{x}^\alpha) = g_0(\mathbf{x}^\alpha) - \left[\mathbf{u}(\mathbf{x}^\alpha) - \mathbf{u}(\mathbf{x}^\beta(\mathbf{x}^\alpha))\right] \cdot \boldsymbol{\nu}(\mathbf{x}^\alpha), \tag{4.11}$$

where $g_0(\mathbf{x}^\alpha) = -\left[\mathbf{x}^\alpha - \mathbf{x}^\beta(\mathbf{x}^\alpha)\right] \cdot \boldsymbol{\nu}(\mathbf{x}^\alpha)$ denotes the initial gap between the two bodies.

Based on the assumptions outlined at the beginning of this section, the gap function g and contact pressure t_N are related through the Kuhn–Tucker complementary conditions:

$$g \leq 0, \qquad t_N \geq 0, \qquad t_N g = 0. \tag{4.12}$$

Equation $(4.12)_1$ reflects the impenetrability of the bodies. Equation $(4.12)_2$ reflects the solely compressive nature of the contact pressure. Equation $(4.12)_3$ reflects that contact pressure is nonzero only if the gap between two points is closed and the two points are separated only if the contact pressure is zero.

The tangential component of the contact traction is governed by Coulomb friction. In other words, the tangential traction may not exceed $\mu_f t_N$ in magnitude. If t_T reaches $\mu_f t_N$ between two contact points, then the points will begin to displace relative to each other along the tangential direction (slip condition). Short of this, however, there will be no relative tangential displacement between the points (stick condition). Introducing the following definitions will help express these frictional constraints symbolically. Let the relative tangential displacement between two contact points be denoted by

$$\psi(\mathbf{x}^\alpha) := \left[\mathbf{u}(\mathbf{x}^\alpha) - \mathbf{u}(\mathbf{x}^\beta(\mathbf{x}^\alpha))\right] \cdot \boldsymbol{\tau}(\mathbf{x}^\beta(\mathbf{x}^\alpha)) \tag{4.13}$$

Let the difference between the tangential traction magnitude and its upper limit, called the trial function, be denoted by

$$\Phi := |t_T| - \mu_f t_N \tag{4.14}$$

With these definitions, the friction constraints may be expressed as follows:

$$\Phi \leq 0, \qquad \operatorname{sign}(\psi) = \operatorname{sign}(t_T), \qquad \Phi\psi = 0. \tag{4.15}$$

Equation $(4.15)_1$ reflects the friction limit on the magnitude of the tangential traction. Equa-

tion $(4.15)_2$ reflects that the direction of the tangential traction vector is opposite the relative displacement after taking into account the convention used for $\boldsymbol{\tau}$. Equation $(4.15)_3$ reflects that relative tangential displacement between two corresponding contact points can be nonzero only if the magnitude of the tangential traction has reached its Coulomb friction limit as a function of the normal traction; conversely, the tangential traction has not reached its friction limit unless the relative tangential displacement is nonzero.

4.1.3 Penalty regularization of mechanical contact constraints

To simplify the numerical solution of such contact problems, the Kuhn–Tucker conditions (4.12) and (4.15) are relaxed by introducing a penalty regularization of the normal and frictional contact constraints. To regularize the normal contact constraint, the normal contact pressure is assumed to vary sharply linearly with the normal component of the interpenetration between the two bodies:

$$t_N = \epsilon_N \langle g \rangle \tag{4.16}$$

Here, ϵ_N is the normal penalty parameter (chosen to be a few orders of magnitude higher than the stiffness of the bodies), g is the familiar gap function, and $\langle \cdot \rangle$ is the Macaulay bracket defined by

$$\langle g \rangle = \begin{cases} g & \text{if } g \geq 0, \\ 0 & \text{otherwise.} \end{cases} \tag{4.17}$$

To regularize the frictional contact constraint, the tangential traction under the stick condition is assumed to vary sharply linearly with the relative tangential displacement:

$$t_T^{\text{stick}} = \epsilon_T \psi \tag{4.18}$$

Here, ϵ_T is the tangential penalty parameter (also chosen to be a few orders of magnitude higher than the stiffness of the bodies).

Whether two corresponding contact points are under the stick or slip condition is determined from the trial state/return mapping algorithm, outlined as follows. First, the stick condition is assumed as the *trial state*, and the trial function (4.14) is computed based on the normal traction from (4.16) and the trial state tangential traction from (4.18). If the trial function is positive, the stick assumption is determined to be incorrect. Thus, in the *return mapping*, the tangential traction is equated to its friction limit. In summary, the trial state/return algorithm based on the regularized contact constraints proceeds as follows:

1. Compute the trial state, assuming the stick condition.

$$\begin{aligned} t_N &= \epsilon_N \langle g \rangle, \\ t_T^{\text{trial}} &= \epsilon_T \psi, \\ \Phi^{\text{trial}} &= |t_T^{\text{trial}}| - \mu_f t_N. \end{aligned} \tag{4.19}$$

2. Check the slip condition.

$$t_T = \begin{cases} t_T^{\text{trial}} & \text{if } \Phi^{\text{trial}} \leq 0 \text{ (stick)}, \\ \mu_f t_N \text{sign}(\psi) & \text{otherwise (slip)}. \end{cases} \tag{4.20}$$

The regularizations of the normal and frictional contact constraints are represented graphically in Figure 4.2.

4.1.4 Thermal contact constraint

The heat flux across the contact interface is assumed to be conductive and to depend on both the contact pressure and the temperature jump between the two bodies at the interface. Based on these assumptions, the following empirical law suggested by [47] is introduced for

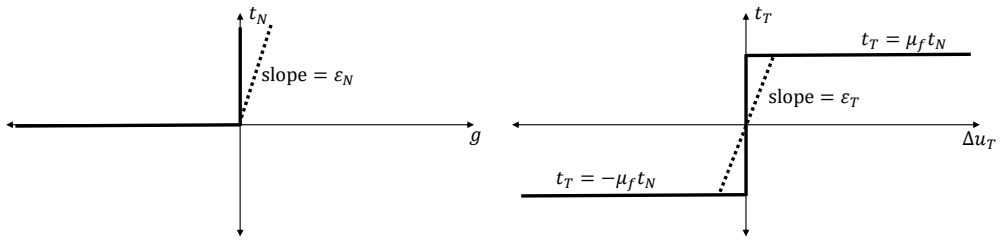

Figure 4.2: Penalty regularization of normal (left) and frictional (right) contact constraints. Solid lines represent the strict Kuhn-Tucker constraints, while dotted lines represent the regularized constraints

the normal heat flux due to contact between $\mathbf{x}^\alpha \in \Gamma_c^\alpha$ and $\mathbf{x}^\beta \in \Gamma_c^\beta$:

$$q^c(\mathbf{x}^\alpha) = h(t_N)\left[\theta(\mathbf{x}^\alpha) - \theta(\mathbf{x}^\beta(\mathbf{x}^\alpha))\right] \tag{4.21}$$

Here, $h(t_N)$ is the pressure-dependent conductivity across the interface. This conductivity is determined using the empirical power law

$$h(t_N) = h_0 \left(\frac{t_N}{H_e}\right)^P \tag{4.22}$$

In (4.22), h_0 is a reference conductivity determined experimentally, P is an exponent determined experimentally, and H_e is the Vickers hardness. The contact pressure t_N is determined from (4.16).

4.2 Discretization of governing equations

The strong form collocation method may be employed in a staggered Newton-Raphson framework to solve the nonlinear problem represented by the governing equations presented in Section 4.1 with the regularized contact constraints from Section 4.1. To develop this approach, we begin by introducing the Newton-Raphson framework to be used in Section 4.2.1, followed by discretizing the governing equations and contact constraints using the

collocation method approximation described in Chapter 2.

4.2.1 Staggered Newton-Raphson scheme

Any nonlinear system of equations may be written as

$$\mathbf{R}(\mathbf{u}) = \mathbf{y}(\mathbf{u}) - \mathbf{f} = \mathbf{0} \tag{4.23}$$

Here, $\mathbf{R}$, called the residual, is a nonlinear mapping of the solution vector $\mathbf{u}$. The terms $\mathbf{y}$ and $\mathbf{f}$ are the non-constant and constant parts of $\mathbf{R}$, respectively. The traditional Newton-Raphson (NR) technique for finding the root $\mathbf{u}$ of this equation is defined by the iterative scheme

$$\mathbf{u}_{k+1} = \mathbf{u}_k - \mathbf{K}_k^{-1}\mathbf{R}(\mathbf{u}_k) \tag{4.24}$$

Of course, an initial guess $\mathbf{u}_0$ is required to begin the iteration. In (4.24), k denotes the iteration step and $\mathbf{K}$, called the tangent stiffness matrix, is defined on the k^{th} step by

$$\mathbf{K} := \frac{\partial \mathbf{R}(\mathbf{u}_k)}{\partial \mathbf{u}} \tag{4.25}$$

It is convenient to denote the update term in (4.24) by

$$\delta\mathbf{u}_k := -\mathbf{K}^{-1}\mathbf{R}(\mathbf{u}_k) \tag{4.26}$$

The iteration in (4.24) is repeated until a desired stopping criterion is reached. A commonly used stopping criterion based on the magnitude of the solution vector update is

$$\text{IF} \quad \frac{||\delta\mathbf{u}_k||}{||\mathbf{u}_k - \mathbf{u}_0||} < TOL, \quad \text{THEN} \quad \text{Stop NR loop.} \tag{4.27}$$

Another commonly used stopping criterion based on the magnitude of the residual is

$$\text{IF} \quad \frac{||\mathbf{R}_k||}{||\mathbf{R}_0||} < TOL, \quad \text{THEN} \quad \text{Stop NR loop.} \tag{4.28}$$

In the context of the present study, the nonlinear system of interest consists of the strong forms of both the mechanical and thermal governing equations, boundary conditions, and contact constraints discretized directly at the collocation points. There are two separate solution vectors in this system. The first is the nodal displacement solution vector given by

$$\mathbf{U} = \begin{bmatrix} u_1^h(\mathbf{x}_1) \\ u_2^h(\mathbf{x}_1) \\ u_1^h(\mathbf{x}_2) \\ u_2^h(\mathbf{x}_2) \\ \vdots \\ u_1^h(\mathbf{x}_N) \\ u_2^h(\mathbf{x}_N) \end{bmatrix} \tag{4.29}$$

The second solution vector is the nodal temperature change vector, given by

$$\mathbf{T} = \begin{bmatrix} \theta^h(\mathbf{x}_1) \\ \theta^h(\mathbf{x}_2) \\ \vdots \\ \theta^h(\mathbf{x}_N) \end{bmatrix} \tag{4.30}$$

Here, $\mathbf{x}_I$ is the I^{th} collocation point, N is the total number of collocation points, u_i^h corresponds to the i^{th} displacement degree of freedom, and T^h corresponds to the temperature change. In the present study, there are a total of three degrees of freedom, namely the x- and y-components of displacement and temperature change. For convenience, $\mathbf{Ui} := \{u_i^h(\mathbf{x}_1), ..., u_i^h(\mathbf{x}_N)\}^T$ will be used to denote the separated solution vectors for the two

degrees of freedom. Note that the shape functions described in 2 do not have the Kronecker delta property, so true values of displacement at the collocation points must be reinterpolated from the nodal solution vector $\mathbf{u}$ using the $(0,0)$ differential operator:

$$u_i(\mathbf{x}_I) \approx \Phi_I^{(0,0)}\mathbf{Ui} \tag{4.31}$$

Similarly, true values of temperature change at the nodes must be reinterpolated according to

$$\theta(\mathbf{x}_I) \approx \Phi_I^{(0,0)}\mathbf{T} \tag{4.32}$$

With this iterative solution framework, the proposed strong form collocation method may be used to determine the appropriate tangent stiffness matrices $\mathbf{K_U}$ and $\mathbf{K_T}$ and residual vectors $\mathbf{R_U}$ and $\mathbf{R_T}$ for the two-body thermo-mechanical contact problem. Using these matrices and vectors, the staggered Newton-Raphson scheme outlined below may be used to determine the solution vectors $\mathbf{U}$ and $\mathbf{T}$:

Staggered Newton-Raphson scheme for thermo-mechanical contact

1. Compute residual vector $\mathbf{R_U}$ and tangent stiffness matrix $\mathbf{K_U}$ using $\mathbf{U}$ and $\mathbf{T}$ from previous iteration.
2. Compute update $\delta\mathbf{U}$ from (4.26) using $\mathbf{R_U}$ and $\mathbf{K_U}$. Update $\mathbf{U}$ according to (4.24).
3. Compute residual vector $\mathbf{R_T}$ and tangent stiffness matrix $\mathbf{K_T}$ using updated $\mathbf{U}$.
4. Compute update $\delta\mathbf{T}$ from (4.26) using $\mathbf{R_T}$ and $\mathbf{K_T}$. Update $\mathbf{T}$ according to (4.24).
5. Check convergence criteria (e.g. (4.27) or (4.28)) separately for $\mathbf{U}$ and $\mathbf{T}$.
6. Repeat steps 1-5 until both convergence criteria are satisfied.

4.2.2 Discretization of mechanical equilibrium and boundary conditions

To determine the discrete form of the equilibrium equations (4.1), the constitutive equation (4.2), and the strain-displacement equations (4.3) and (4.4) are substituted in (4.1) to yield

$$\mu\Delta\mathbf{u} + (\lambda+\mu)\nabla(\nabla\cdot\mathbf{u}) - 2\alpha_v'(\lambda+\mu)\nabla\theta + \mathbf{b} = 0 \quad \text{in } \Omega \tag{4.33}$$

Here, plane strain is assumed, so that the Lamé constants are given by

$$\begin{aligned} \lambda &= \frac{\nu E}{(1-2\nu)(1+\nu)} \\ \mu &= \frac{E}{2(1+\nu)} \end{aligned} \tag{4.34}$$

where E is Young's modulus, and ν is Poisson's ratio (not to be confused with $\boldsymbol{\nu}$, the contact normal vector). Note that a modified plane strain coefficient of thermal expansion $\alpha_v' = (1+\nu)\alpha_v$ is used in (4.33). In index notation for Cartesian components, (4.33) is written equivalently as

$$\mu u_{i,jj} + (\lambda+\mu)u_{j,ji} - 2\alpha_v'(\lambda+\mu)\theta_{,i} + b_i = 0 \quad \text{in } \Omega \tag{4.35}$$

where $i, j = 1, 2$ in two dimensions and repeated indices obey the summation convention. When these equations are expanded explicitly, they become the pair of equations

$$\begin{aligned} &(\lambda+2\mu)u_{1,11} + \mu u_{1,22} + (\lambda+\mu)u_{2,21} - 2\alpha_v'(\lambda+\mu)\theta_{,1} + b_1 = 0 \\ &(\lambda+\mu)u_{1,12} + (\lambda+2\mu)u_{2,22} + \mu u_{2,11} - 2\alpha_v'(\lambda+\mu)\theta_{,2} + b_2 = 0 \end{aligned} \tag{4.36}$$

The strong form of the PDEs in (4.36) are discretized by replacing the various derivative terms with approximate derivatives constructed using the differential operators from Chapter 2. This discretization is used to construct the equations for each interior collocation point. Suppose $\mathbf{x}_I \in \Omega$ is an interior collocation point and let $\Phi_{IJ}^{\boldsymbol{\alpha}}$ represent the J^{th} entry of the $\boldsymbol{\alpha}^{\text{th}}$

differential operator at collocation point $\mathbf{x}_I$. Then the equations in (4.36) for node $\mathbf{x}_I \in \Omega$ are discretized as

$$\begin{aligned} R_{I1}^{\text{intU}} :=& \sum_{J=1}^{N} \left[\left((\lambda + 2\mu)\Phi_{IJ}^{(2,0)} + \mu\Phi_{IJ}^{(0,2)} \right) u_1^h(\mathbf{x}_J) + \left((\lambda + \mu)\Phi_{IJ}^{(1,1)} \right) u_2^h(\mathbf{x}_J) \right] \\ & - \sum_{J=1}^{N} \left(2\alpha_v'(\lambda + \mu)\Phi_{IJ}^{(1,0)} \right) \theta^h(\mathbf{x}_J) + b_1(\mathbf{x}_I) \\ R_{I2}^{\text{intU}} :=& \sum_{J=1}^{N} \left[\left((\lambda + \mu)\Phi_{IJ}^{(1,1)} \right) u_1^h(\mathbf{x}_J) + \left((\lambda + 2\mu)\Phi_{IJ}^{(0,2)} + \mu\Phi_{IJ}^{(2,0)} \right) u_2^h(\mathbf{x}_J) \right] \\ & - \sum_{J=1}^{N} \left(2\alpha_v'(\lambda + \mu)\Phi_{IJ}^{(0,1)} \right) \theta^h(\mathbf{x}_J) + b_2(\mathbf{x}_I) \end{aligned} \tag{4.37}$$

Thus, for node $\mathbf{x}_I \in \Omega$, the 2×2 IJ block of $\mathbf{K_U}$ is given by the partial derivative of (4.37) with respect to $\{u_1^h(\mathbf{x}_J), u_2^h(\mathbf{x}_J)\}$, i.e.,

$$\mathbf{K}_{IJ}^{\text{intU}} = \begin{bmatrix} (\lambda + 2\mu)\Phi_{IJ}^{(2,0)} + \mu\Phi_{IJ}^{(0,2)} & (\lambda + \mu)\Phi_{IJ}^{(1,1)} \\ (\lambda + \mu)\Phi_{IJ}^{(1,1)} & (\lambda + 2\mu)\Phi_{IJ}^{(0,2)} + \mu\Phi_{IJ}^{(2,0)} \end{bmatrix} \tag{4.38}$$

Note that the derivatives of the residual with respect to the nodal temperatures are not included due to the staggered coupling scheme.

Substituting (4.2) and (4.3) in (4.7), the traction condition can be expressed in index notation as

$$\sigma_{ij} n_j - \bar{t}_i = \lambda u_{j,j} n_i + \mu(u_{i,j} + u_{j,i}) n_j - 2\alpha_v'(\lambda + \mu)\theta n_i - \bar{t}_i = 0 \tag{4.39}$$

This is expanded as

$$\begin{aligned} &(\lambda + 2\mu)n_1 u_{1,1} + \mu n_2 u_{1,2} + \lambda n_1 u_{2,2} + \mu n_2 u_{2,1} && - 2\alpha_v'(\lambda + \mu)\theta n_1 - \bar{t}_1 = 0 \\ &\lambda n_2 u_{1,1} + \mu n_1 u_{1,2} && + (\lambda + 2\mu)n_2 u_{2,2} + \mu n_1 u_{2,1} - 2\alpha_v'(\lambda + \mu)\theta n_2 - \bar{t}_2 = 0 \end{aligned} \tag{4.40}$$

Then, following the example of the interior nodes, if $\mathbf{x}_I \in \Gamma_t^\alpha$ is a prescribed traction boundary

node, the discretized equation at node $\mathbf{x}_I$ is expressed as

$$\begin{aligned}
R_{I1}^{\text{trac}} :=& \sum_{J=1}^{N} \left[\left((\lambda + 2\mu) n_1 \Phi_{IJ}^{(1,0)} + \mu n_2 \Phi_{IJ}^{(0,1)} \right) u_1^h(\mathbf{x}_J) + \left(\lambda n_1 \Phi_{IJ}^{(0,1)} + \mu n_2 \Phi_{IJ}^{(1,0)} \right) u_2^h(\mathbf{x}_J) \right] \\
& - \sum_{J=1}^{N} \left(2\alpha_v'(\lambda + \mu) n_1 \Phi_{IJ}^{(0,0)} \right) \theta^h(\mathbf{x}_J) - \bar{t}_1(\mathbf{x}_I) \\
R_{I2}^{\text{trac}} :=& \sum_{J=1}^{N} \left[\left(\lambda n_2 \Phi_{IJ}^{(1,0)} + \mu n_1 \Phi_{IJ}^{(0,1)} \right) u_1^h(\mathbf{x}_J) + \left((\lambda + 2\mu) n_2 \Phi_{IJ}^{(0,1)} + \mu n_1 \Phi_{IJ}^{(1,0)} \right) u_2^h(\mathbf{x}_J) \right] \\
& - \sum_{J=1}^{N} \left(2\alpha_v'(\lambda + \mu) n_2 \Phi_{IJ}^{(0,0)} \right) \theta^h(\mathbf{x}_J) - \bar{t}_2(\mathbf{x}_I)
\end{aligned} \tag{4.41}$$

For convenience in discretizing the contact constraints in Section 4.2.3, the non-constant part of (4.41) will be denoted

$$\mathbf{y}_I^{\text{trac}} := \mathbf{R}_I^{\text{trac}} + \bar{\mathbf{t}}(\mathbf{x}_I) \tag{4.42}$$

Each corresponding IJ block of the tangent stiffness $\mathbf{K}_{\mathbf{U}}$ for $\mathbf{x}_I \in \Gamma_t^\alpha$ is then given by

$$\mathbf{K}_{IJ}^{\text{trac}} = \begin{bmatrix} (\lambda + 2\mu) n_1 \Phi_{IJ}^{(1,0)} + \mu n_2 \Phi_{IJ}^{(0,1)} & \lambda n_1 \Phi_{IJ}^{(0,1)} + \mu n_2 \Phi_{IJ}^{(1,0)} \\ \lambda n_2 \Phi_{IJ}^{(1,0)} + \mu n_1 \Phi_{IJ}^{(0,1)} & (\lambda + 2\mu) n_2 \Phi_{IJ}^{(0,1)} + \mu n_1 \Phi_{IJ}^{(1,0)} \end{bmatrix} \tag{4.43}$$

Finally, if $\mathbf{x}_I \in \Gamma_u^\alpha$ is a prescribed displacement boundary node, the discretized equation at node $\mathbf{x}_I$ is simply expressed as

$$\begin{aligned}
R_{I1}^{\text{disp}} &:= \sum_{J=1}^{N} \Phi_{IJ}^{(0,0)} u_1^h(\mathbf{x}_J) - \bar{u}_1 \\
R_{I2}^{\text{disp}} &:= \sum_{J=1}^{N} \Phi_{IJ}^{(0,0)} u_2^h(\mathbf{x}_J) - \bar{u}_2
\end{aligned} \tag{4.44}$$

Each corresponding IJ block of the tangent stiffness $\mathbf{K_U}$ for $\mathbf{x}_I \in \Gamma_u^\alpha$ is then given by

$$\mathbf{K}_{IJ}^{\text{disp}} = \begin{bmatrix} \Phi_{IJ}^{(0,0)} & 0 \\ 0 & \Phi_{IJ}^{(0,0)} \end{bmatrix} \tag{4.45}$$

In the event that there is a mixed boundary condition at a node, e.g., a roller boundary condition, the appropriate discretized equations can be formulated as a suitable hybrid of (4.41) and (4.44). Given these discretized boundary conditions and governing PDE for the interior nodes (4.37), the full tangent stiffness matrix and residual vector are almost ready to be assembled. Notice that the equations developed so far are linear due to the linear elastic constitutive law and small displacement and strain assumption. The nonlinearity for the contact problem in this study comes solely from the contact constraints, discretized in the following section.

4.2.3 Discretization of regularized mechanical contact constraints

Like the traction boundary condition $(4.7)_2$, the contact condition $(4.7)_3$ contains the $\boldsymbol{\sigma}\mathbf{n}$ term. Unlike prescribed traction $\bar{\mathbf{t}}$, however, the contact traction $\mathbf{t}^c$ depends on the displacement field. To discretize the contact constraints, we begin by substituting (4.10) in $(4.7)_3$ and writing this equation in index notation:

$$\sigma_{ij} n_j - t_i^c = \lambda u_{j,j} n_i + \mu(u_{i,j} + u_{j,i}) n_j - t_N \nu_i + t_T \tau_i = 0 \tag{4.46}$$

The values of contact pressure t_N and tangential traction t_T depend on the gap function and the slip/stick state of the system, as explained in Section 4.1. The gap function is discretized in terms of both the primary contact node $\mathbf{x}_I^\alpha \in \Gamma_c^\alpha$ and the corresponding contact node $\mathbf{x}_I^\beta \in \Gamma_c^\beta$ as follows:

$$g(\mathbf{x}_I^\alpha) \approx G_I := g_0(\mathbf{x}_I^\alpha) - \sum_{J=1}^{N} \left(\Phi_{IJ}^{(0,0)} - \Phi_{I'J}^{(0,0)} \right) \left[\nu_1 u_1^h(\mathbf{x}_J) + \nu_2 u_2^h(\mathbf{x}_J) \right] \tag{4.47}$$

Here, $\Phi_{IJ}^{(0,0)}$ is the reinterpolation operator for $\mathbf{x}_I^\alpha$, while $\Phi_{I'J}^{(0,0)}$ is the reinterpolation operator for $\mathbf{x}_I^\beta$. The initial gap g_0 is known *a priori* based on the undeformed geometry of the problem. Similarly, the relative tangential displacement is discretized as follows:

$$\psi(\mathbf{x}_I^\alpha) \approx \Psi_I := \sum_{J=1}^{N} \left(\Phi_{IJ}^{(0,0)} - \Phi_{I'J}^{(0,0)} \right) \left[\tau_1 u_1^h(\mathbf{x}_J) + \tau_2 u_2^h(\mathbf{x}_J) \right] \tag{4.48}$$

In the event that the bodies are not in contact (i.e. $g < 0$) at two corresponding contact points, there is neither contact pressure nor tangential traction between the bodies at those points. Thus, for a node $\mathbf{x}_I \in \Gamma_c^\alpha$ for which $g < 0$,

$$\begin{aligned} R_{I1}^{g<0} &:= y_{I1}^{\text{trac}} \\ R_{I2}^{g<0} &:= y_{I2}^{\text{trac}} \end{aligned} \tag{4.49}$$

Here, $\mathbf{y}_I^{\text{trac}}$ is given by (4.42). Each corresponding IJ block of $\mathbf{K_U}$ is given by

$$\mathbf{K}_{IJ}^{g<0} = \mathbf{K}_{IJ}^{\text{trac}} \tag{4.50}$$

Notice that this case is equivalent to a traction-free boundary condition.

If the gap between two corresponding contact points $\mathbf{x}_I^\alpha \in \Gamma_c^\alpha$ and $\mathbf{x}_I^\beta \in \Gamma_c^\beta$ is closed and the points are under the stick condition, then substituting (4.16) and (4.18) in (4.46), expanding, and applying the differential operators yields

$$\begin{aligned} R_{I1}^{stick} &:= y_{I1}^{\text{trac}} - \epsilon_N G_I \nu_1 + \epsilon_T \Psi_I \tau_1 \\ R_{I2}^{stick} &:= y_{I2}^{\text{trac}} - \epsilon_N G_I \nu_2 + \epsilon_T \Psi_I \tau_2 \end{aligned} \tag{4.51}$$

Note that the terms involving the gap function have been discretized using (4.47). Differentiating the normal and tangential traction terms with respect to u_1^h and u_2^h leads to the

expression for the IJ blocks of $\mathbf{K_U}$ for each $\mathbf{x}_I^\alpha \in \Gamma_c^\alpha,\ \alpha \in \{1,2\}$:

$$\mathbf{K}_{IJ}^{stick} = \mathbf{K}_{IJ}^{\text{trac}} - \epsilon_N \left(\Phi_{IJ}^{(0,0)} - \Phi_{I'J}^{(0,0)}\right) \begin{bmatrix} \nu_1\nu_1 & \nu_1\nu_2 \\ \nu_2\nu_1 & \nu_2\nu_2 \end{bmatrix} + \epsilon_T \left(\Phi_{IJ}^{(0,0)} - \Phi_{I'J}^{(0,0)}\right) \begin{bmatrix} \tau_1\tau_1 & \tau_1\tau_2 \\ \tau_2\tau_1 & \tau_2\tau_2 \end{bmatrix} \tag{4.52}$$

Finally, if the gap between $\mathbf{x}_I^\alpha$ and $\mathbf{x}_I^\beta$ is closed and the two points are under the slip condition, then substituting (4.16) and (4.20) in (4.46), expanding, and applying the differential operators yields

$$\begin{aligned} R_{I1}^{slip} &:= y_{I1}^{\text{trac}} - \epsilon_N G_I \nu_1 + \mu_f \epsilon_N G_I \text{sign}(\Psi_I)\tau_1 \\ R_{I2}^{slip} &:= y_{I2}^{\text{trac}} - \epsilon_N G_I \nu_2 + \mu_f \epsilon_N G_I \text{sign}(\Psi_I)\tau_2 \end{aligned} \tag{4.53}$$

Each corresponding block IJ of $\mathbf{K_U}$ in the case of stick is then given by

$$\begin{aligned} \mathbf{K}_{IJ}^{slip} =& \mathbf{K}_{IJ}^{\text{trac}} - \epsilon_N \left(\Phi_{IJ}^{(0,0)} - \Phi_{I'J}^{(0,0)}\right) \begin{bmatrix} \nu_1\nu_1 & \nu_1\nu_2 \\ \nu_2\nu_1 & \nu_2\nu_2 \end{bmatrix} \\ &+ \mu_f \epsilon_N \text{sign}(\Psi_I) \left(\Phi_{IJ}^{(0,0)} - \Phi_{I'J}^{(0,0)}\right) \begin{bmatrix} \tau_1\nu_1 & \tau_1\nu_2 \\ \tau_2\nu_1 & \tau_2\nu_2 \end{bmatrix} \end{aligned} \tag{4.54}$$

In summary, each portion of the residual vector and block of the tangent stiffness matrix corresponding to a contact collocation point $\mathbf{x}_I^\alpha \in \Gamma_c^\alpha,\ \alpha \in \{1,2\}$ is given by

$$\mathbf{R}_I^{\text{contU}} = \begin{cases} \mathbf{R}_I^{\text{gi0}}, & \text{if } g < 0 \\ \mathbf{R}_I^{\text{stick}}, & \text{if stick} \\ \mathbf{R}_I^{\text{slip}}, & \text{if slip} \end{cases} \tag{4.55}$$

Each IJ block of the contact condition part of $\mathbf{K_U}$ is given by

$$\mathbf{K}_{IJ}^{\text{contU}} = \begin{cases} \mathbf{K}_{IJ}^{\text{gi0}}, & \text{if } g < 0 \\ \mathbf{K}_{IJ}^{\text{stick}}, & \text{if stick} \\ \mathbf{K}_{IJ}^{\text{slip}}, & \text{if slip} \end{cases} \tag{4.56}$$

These expressions (4.55) and (4.56) may be used in conjunction with the discretized equations in Section 4.2.2 to assemble the total residual vector and tangent stiffness matrix for the problem. No special method of assembly is required, unlike in the context of finite elements; the expressions developed above are simply concatenated $I = 1 : N$ according to the type (interior, boundary, contact, etc.) of node I. Thus, the I^{th} block of $\mathbf{R_U}$, i.e. entries $2I - 1$ and $2I$ of $\mathbf{R_U}$, is given by

$$(\mathbf{R_U})_I = \begin{cases} \mathbf{R}_I^{\text{intU}}, & \text{if } \mathbf{x}_I \in \Omega \\ \mathbf{R}_I^{\text{trac}}, & \text{if } \mathbf{x}_I \in \Gamma_t \\ \mathbf{R}_I^{\text{disp}}, & \text{if } \mathbf{x}_I \in \Gamma_u \\ \mathbf{R}_I^{\text{contU}}, & \text{if } \mathbf{x}_I \in \Gamma_c \end{cases} \tag{4.57}$$

Similarly, the IJ block of $\mathbf{K_U}$ is given by

$$(\mathbf{K_U})_{IJ} = \begin{cases} \mathbf{K}_{IJ}^{\text{intU}}, & \text{if } \mathbf{x}_I \in \Omega \\ \mathbf{K}_{IJ}^{\text{trac}}, & \text{if } \mathbf{x}_I \in \Gamma_t \\ \mathbf{K}_{IJ}^{\text{disp}}, & \text{if } \mathbf{x}_I \in \Gamma_u \\ \mathbf{K}_{IJ}^{\text{contU}}, & \text{if } \mathbf{x}_I \in \Gamma_c \end{cases} \tag{4.58}$$

Note that the tangent stiffness matrix $\mathbf{K_U}$ is discontinuous at the transitions between non-contact and contact, and between stick and slip. For this reason, the Newton-Raphson

iteration using $\mathbf{R_U}$ and $\mathbf{K_U}$ is not guaranteed to converge mathematically. However, in practice, this process does converge for the problems considered in this study, so smoother regularizations of the contact pressure and tangential traction are not considered. It would be straightforward to modify these expressions to have continuous first and second derivatives using, for example, Hermite interpolation of contact pressure and tangential traction in a user-defined radius around $g = 0$, $\psi = 0$, and $\Phi^{\text{trial}} = 0$.

4.2.4 Discretization of thermal equations

The thermal governing equation, boundary conditions, and contact constraints are discretized in a similar fashion. When (4.6) is substituted in (4.5) and expanded, the result is Poisson's equation:

$$-\kappa \left(\theta_{,11} + \theta_{,22}\right) + s = 0 \tag{4.59}$$

Thus, for an interior collocation point $\mathbf{x}_I \in \Omega$, this is discretized as

$$R_I^{\text{intT}} := \sum_{J=1}^{N} \left[-\kappa \left(\Phi_{IJ}^{(2,0)} + \Phi_{IJ}^{(0,2)} \right) \theta^h(\mathbf{x}_J) \right] + s(\mathbf{x}_I) \tag{4.60}$$

The IJ entry of $\mathbf{K_T}$ corresponding to $\mathbf{x}_I \in \Omega$ is then given by

$$K_{IJ}^{\text{intT}} = -\kappa \left(\Phi_{IJ}^{(2,0)} + \Phi_{IJ}^{(0,2)} \right) \tag{4.61}$$

The prescribed heat flux boundary condition is expanded to yield

$$-\kappa \left(\theta_{,1} n_1 + \theta_{,2} n_2\right) - \bar{q} = 0 \tag{4.62}$$

Thus, for a prescribed heat flux boundary point $\mathbf{x}_I \in \Gamma_q$, this is discretized as

$$R_I^{\text{flux}} := \sum_{J=1}^{N} \left[-\kappa \left(\Phi_{IJ}^{(1,0)} n_1 + \Phi_{IJ}^{(0,1)} n_2 \right) \theta^h(\mathbf{x}_J) \right] - \bar{q}(\mathbf{x}_I) \tag{4.63}$$

For convenience in discretizing the contact condition, let $y_I^{\text{flux}} = R_I^{\text{flux}} + \bar{q}(\mathbf{x}_I)$. The IJ entry of $\mathbf{K_T}$ corresponding to $\mathbf{x}_I \in \Gamma_q$ is then given by

$$K_{IJ}^{\text{flux}} = -\kappa \left(\Phi_{IJ}^{(1,0)} n_1 + \Phi_{IJ}^{(0,1)} n_2 \right) \tag{4.64}$$

The discretized equation for a prescribed temperature boundary collocation point $\mathbf{x}_I \in \Gamma_\theta$ is simply given by

$$R_I^{\text{temp}} := \sum_{J=1}^{N} \left[\Phi_{IJ}^{(0,0)} \theta^h(\mathbf{x}_J) \right] - \bar{\theta}(\mathbf{x}_I) \tag{4.65}$$

The IJ entry of $\mathbf{K_T}$ corresponding to $\mathbf{x}_I \in \Gamma_\theta$ is then given by

$$K_{IJ}^{\text{temp}} = \Phi_{IJ}^{(0,0)} \tag{4.66}$$

Finally, if $\mathbf{x}_I^\alpha \in \Gamma_c^\alpha$ is a contact node and $\mathbf{x}_I^\beta \in \Gamma_c^\beta$ is its corresponding contact node on the other body, the discretized form of the thermal contact condition is given by

$$R_I^{\text{contT}} := y_I^{\text{flux}} - \sum_{J=1}^{N} \left[h_0 \left(\frac{\epsilon_N \langle G_I \rangle}{H_e} \right)^P \left(\Phi_{IJ}^{(0,0)} - \Phi_{I'J}^{(0,0)} \right) \theta^h(\mathbf{x}_J) \right] \tag{4.67}$$

Here, as in the discretized mechanical contact constraints, G_I is the discretized gap function (4.47) and $\Phi_{IJ}^{(0,0)}$ and $\Phi_{I'J}^{(0,0)}$ are the reinterpolation operators for $\mathbf{x}_I^\alpha$ and $\mathbf{x}_I^\beta$ respectively. Again recalling that the derivative terms with respect to the nodal displacement solution vector are neglected because this study is considering a staggered Newton-Raphson scheme, the IJ entry of the tangent stiffness $\mathbf{K_T}$ is given by

$$K_{IJ}^{\text{contT}} := K_{IJ}^{\text{flux}} - h_0 \left(\frac{\epsilon_N \langle G_I \rangle}{H_e} \right)^P \left(\Phi_{IJ}^{(0,0)} - \Phi_{I'J}^{(0,0)} \right) \tag{4.68}$$

The full residual vector $\mathbf{R_T}$ and tangent stiffness matrix $\mathbf{K_T}$ are assembled in similar fashion as (4.57) and (4.58).

4.3 Numerical study

In this section, the proposed nonlinear strong form collocation method is verified through two numerical examples related to two-body mechanical contact alone and one related to thermomechanical contact. The first, involving frictional contact between two blocks along an inclined surface, is used to assess the ability of the proposed method to distinguish between slip and stick conditions. The second, involving Hertzian contact between two half-cylinders, verifies the method against a nontrivial analytical solution. The third, involving thermomechanical contact between two rectangular blocks, verifies the pressure-dependent thermal contact model and that the mechanical and thermal problems may be accurately solved together using the staggered Newton-Raphson scheme.

4.3.1 Mechanical contact along an inclined surface

The first numerical example considered in this study concerns mechanical contact between two blocks along an inclined surface. A version of this example was used in [56] to verify a mortared finite element method for multi-body frictional contact. The geometry for this problem is shown in Figure 4.3. In their reference configuration, the two blocks together form a square of side length 2.0. They are separated by a contact surface of frictional coefficient μ_f along a line of slope $m = 0.2$ through the centroid of the square. The block below the contact surface is pinned at the bottom right corner and resting on rollers along the remainder of its bottom surface. The top block has a prescribed displacement of $u_y = -0.01$ at its top surface. It is restrained in the x-direction at the top right corner but free in the x-direction along the rest of the top surface. The left and right sides of the block are traction-free. For both blocks, the Young's modulus and Poisson's ratio are $E = 1.0$ and $\nu = 0.3$. The normal and tangential penalty parameters are chosen to be $\epsilon_N = \epsilon_T = 1.0 \times 10^6 E$ (as for the rest of the numerical examples in this section unless otherwise stated).

The purpose of this numerical example is to determine with what sensitivity the proposed

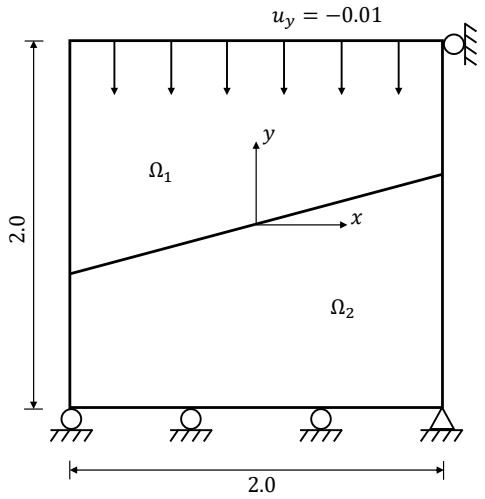

Figure 4.3: Free-body diagram for the problem of mechanical contact along an inclined surface

method can distinguish between the slip and stick conditions. Theoretically, if the coefficient of friction μ_f is chosen to be greater than the slope of the interface m, then the entire contact surface will be under the stick condition. Conversely, if μ_f is chosen to be less than the slope of the contact interface, then the entire contact surface will be under the slip condition. However, in practice, there will be some threshold coefficient of friction $\mu_{\text{thresh}} \neq m$ above which the contact surface sticks and below which it slips. Thus, how small a difference exists between μ_{thresh} and m is a measure of the sensitivity with which the method can distinguish between stick and slip.

Figure 4.4 shows an example arrangement of collocation points used for this problem. This arrangement is a uniform Cartesian-product grid perturbed so that the number of contact points along the inclined surface is equal to the number of points along the bottom edge of the domain. Using the nodal arrangement shown in Figure 4.4, the displacement field is computed using the proposed method for various values of the friction coefficient μ_f near 0.2. The results of these trials indicate that the threshold friction coefficient for the proposed method is $\mu_{\text{thresh}} = 0.1999997 = m - (3 \times 10^{-7})$. Contour plots of the displacement field are shown for $\mu_f = 0.19$ in Figure 4.5 and for $\mu_f = 0.21$ in Figure 4.6. Slip is clearly

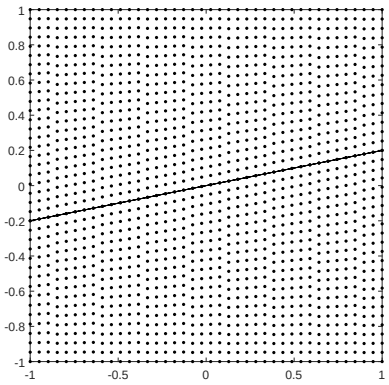

Figure 4.4: Example arrangement of collocation points for the inclined surface problem

visible in the discontinuity in the u_1 field for $\mu_f = 0.19$ in Figure 4.5.

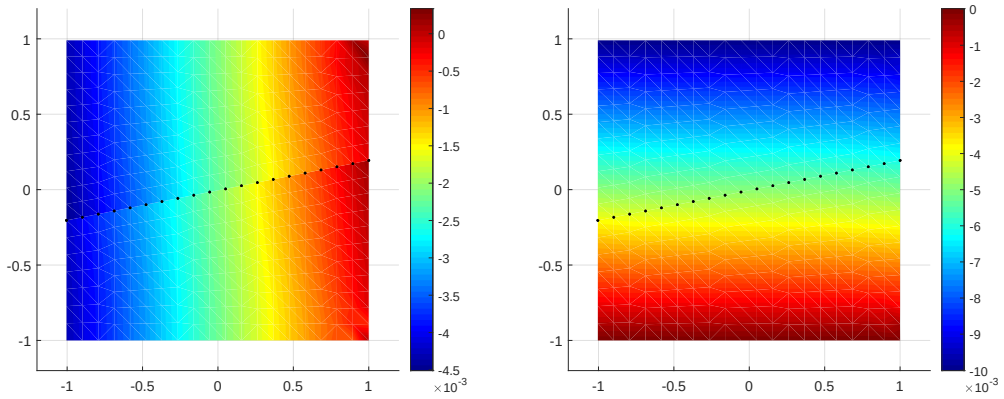

(a) (b)

Figure 4.5: (a) x-component and (b) y-component of displacement for the inclined surface problem, $\mu_f = 0.19$

In order to verify the results of the proposed method for the inclined contact surface example, the contact pressure and tangential traction computed from the method are compared with results from FEM. In addition to the sum of normal contact tractions from each side of the interface (which should be zero in equilibrium), Figures 4.7 and 4.8 shows the contact pressure profile along the contact surface according to the stress field, the contact algorithm, and an `ABAQUS` FEM model. The FEM model was chosen to have roughly the

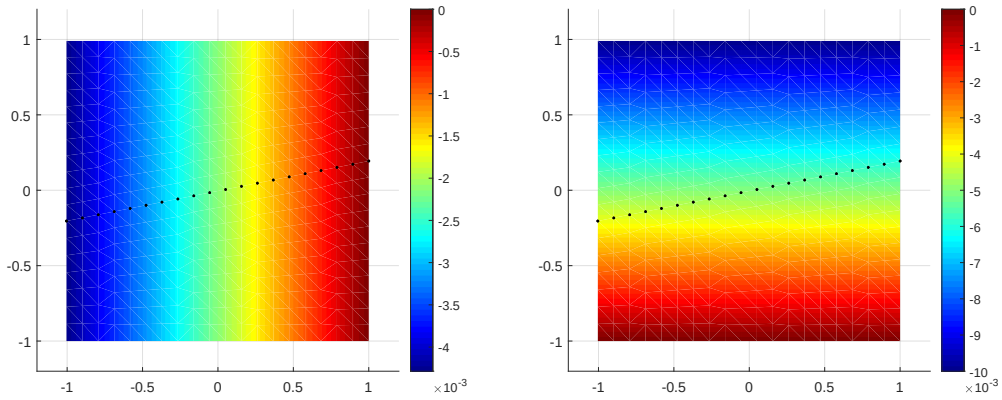

(a) (b)

Figure 4.6: (a) x-component and (b) y-component of displacement for the inclined surface problem, $\mu_f = 0.21$

same level of discretization as the collocation point arrangement in Figure 4.4.

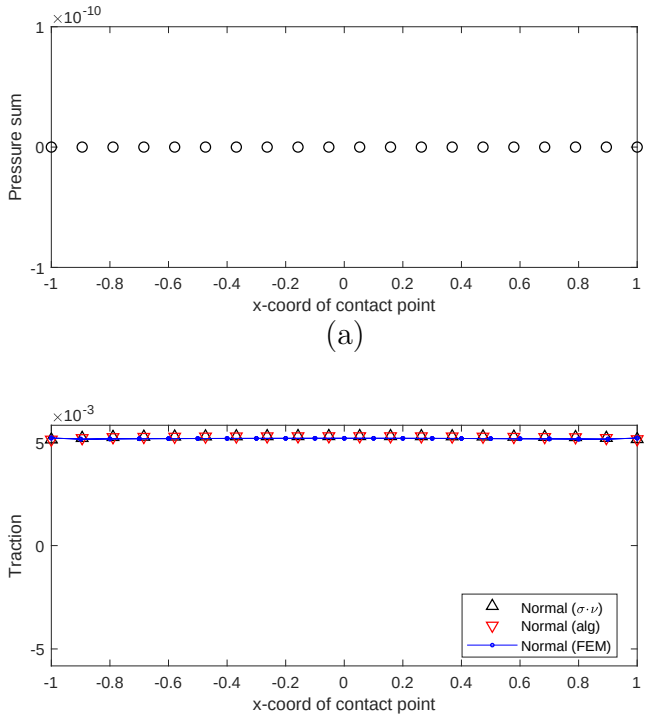

Figure 4.7: (a) Sum of normal tractions from top and bottom surface of contact interface and (b) contact pressure from stress, contact algorithm, and FEM for $\mu_f = 0.19$

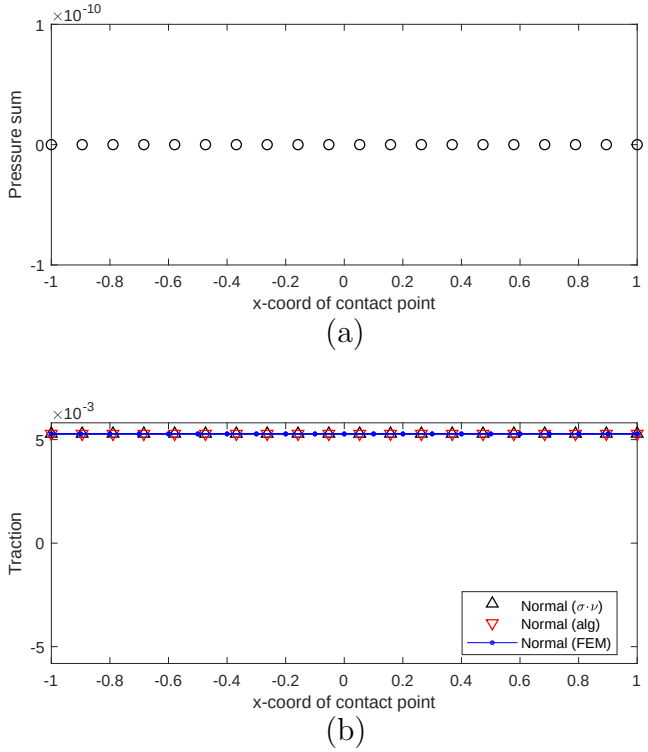

Figure 4.8: (a) Sum of normal tractions from top and bottom surface of contact interface and (b) contact pressure from stress, contact algorithm, and FEM for $\mu_f = 0.21$

A similar comparison is shown in Figures 4.9 and 4.10. For both contact pressure and tangential traction, the results from different parts of the proposed method algorithm agree with each other and with the FEM model.

4.3.2 Hertzian contact between two half-cylinders

The second numerical example considered in this study concerns Hertzian contact between two half-cylinders. A version of this example was used in [54] for verification purposes. The geometry for this problem is shown in Figure 4.11. As shown, two half-cylinders of radius $R = 8$ are in kissing contact at the origin. They are separated by a flat contact surface of frictional coefficient $\mu_f = 0.2$. The bottom edge of the bottom half-cylinder is fixed in both directions. The top block has a prescribed displacement of $\bar{\mathbf{u}}(x) = \{\bar{u}_x(x), \bar{u}_y(x)\}$ along its top surface. All other boundaries (other than the contact interface) are traction-free. For

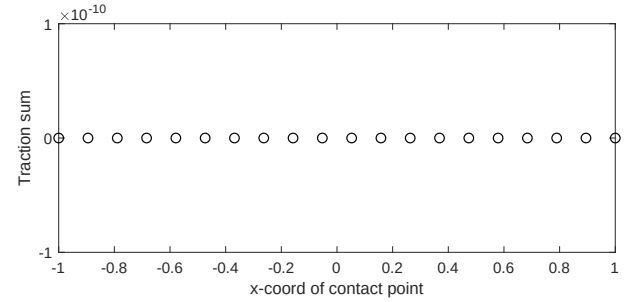

(a)

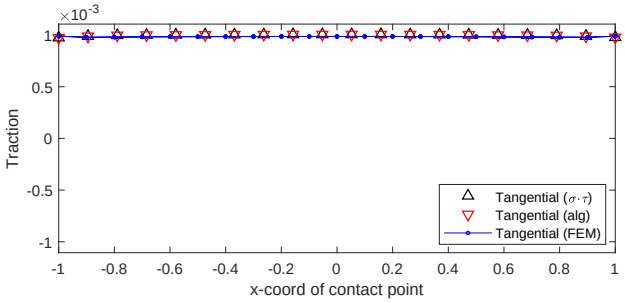

(b)

Figure 4.9: (a) Sum of tangential tractions from top and bottom surface of contact interface and (b) tangential traction from stress, contact algorithm, and FEM for $\mu_f = 0.19$

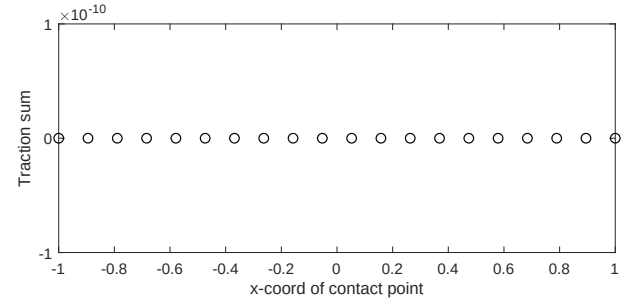

(a)

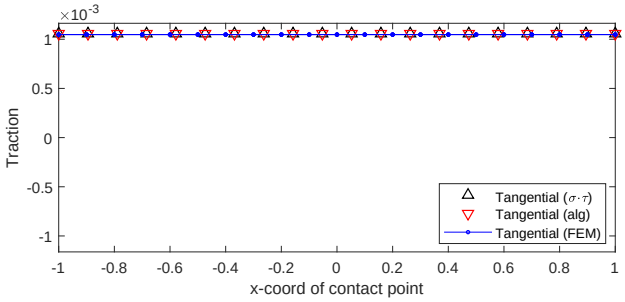

(b)

Figure 4.10: (a) Sum of tangential tractions from top and bottom surface of contact interface and (b) tangential traction from stress, contact algorithm, and FEM for $\mu_f = 0.21$

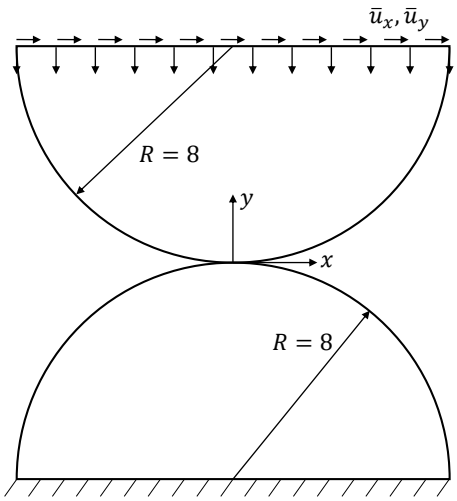

Figure 4.11: Free-body diagram for Hertzian contact problem

both bodies, the Young's modulus and Poisson's ratio are $E = 200$ and $\nu = 0.3$. The normal and tangential penalty parameters are again chosen to be $\epsilon_N = \epsilon_T = 1.0 \times 10^4 E$.

The arrangement of collocation points used for this problem is shown in Figure 4.12. It is a random arrangement of points generated using the open-source meshing software `gmsh`. The spacing of collocation points around the contact point is much smaller than that in the rest of the domain to ensure a sufficient number of contact nodes and local precision of the solution.

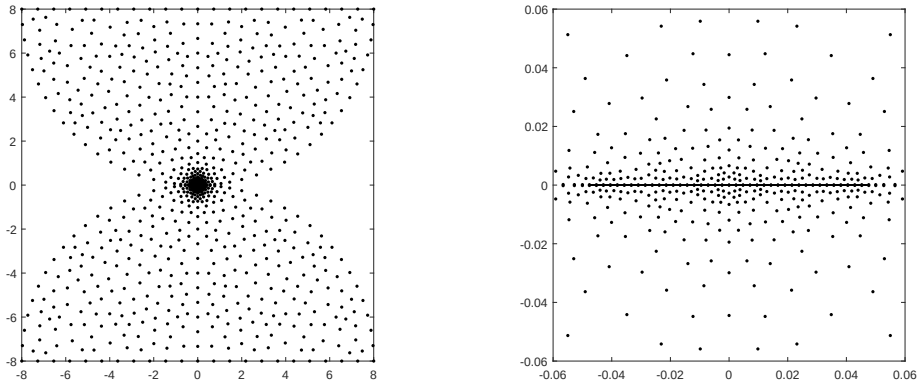

(a) (b)

Figure 4.12: (a) Arrangement of collocation points for the Hertzian contact problem and (b) Detail of nodal arrangement near contact surface

Before applying both horizontal and vertical loads to the top edge of the top cylinder, a simplified case is considered in which $\mu_f = 0$ and only vertical loading is applied. Under these conditions, $x = 0$ is a line of symmetry, allowing half the problem to be considered. When only half the problem is considered, the numerical algorithm proposed here is sufficiently stable that a vertical traction may be considered at the top surface. (When the full problem is considered, the algorithm becomes unstable because the top cylinder is not sufficiently constrained and undergoes uncontrolled rigid body motion). For the Hertzian contact problem with only vertical traction loading, an analytical solution is available. Thus, we can use this example to compare the results from the proposed method with an analytical solution for a problem in which the contact traction distribution is nontrivial. The analytical solution for contact pressure along the contact surface was provided by [65] and is given by the elliptical profile

$$t_N(x) = \frac{2p_{\text{top}}}{\pi a^2}\left(a^2 - x^2\right)^{1/2} \tag{4.69}$$

Here, p_{top} is the prescribed normal traction at the top edge. The value of a is found from

$$a = \sqrt{\frac{4p_{\text{top}}R}{\pi E}} \tag{4.70}$$

In (4.70), R is the radius of the cylinder and E is the Young's modulus of the cylinders. Contour plots of the x- and y-components of displacement computed using the proposed method are given in Figure 4.13. A comparison between the contact pressure computed from the proposed method and that from the exact solution is shown in Figure 4.14. Figure 4.14 shows agreement between the proposed method and the exact solution, particularly with respect to the peak contact pressure. There is higher error in the contact pressure near the edge of the contact boundary. However, as the collocation point arrangement is further refined, the discrepancy between the computed and analytical solution near the edge of the contact boundary is reduced. It should also be noted that finite element methods such as [55] experience similar difficulties.

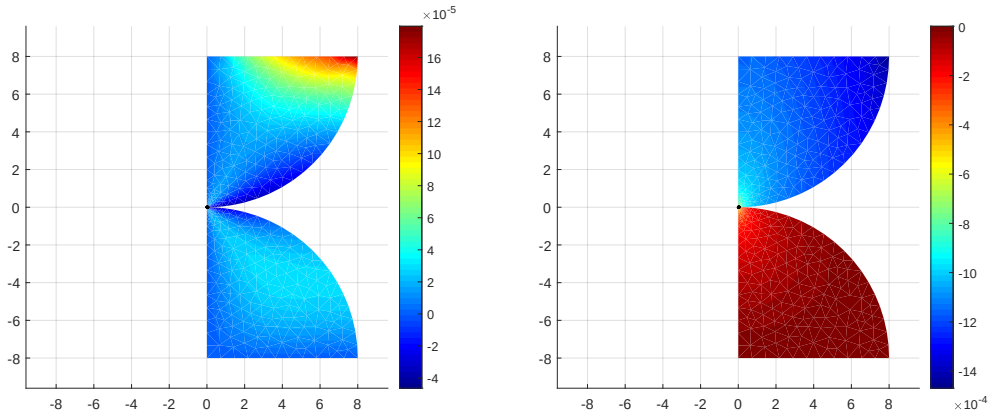

(a) (b)

Figure 4.13: (a) x-component and (b) y-component of displacement for the half-Hertzian contact problem according to the proposed method

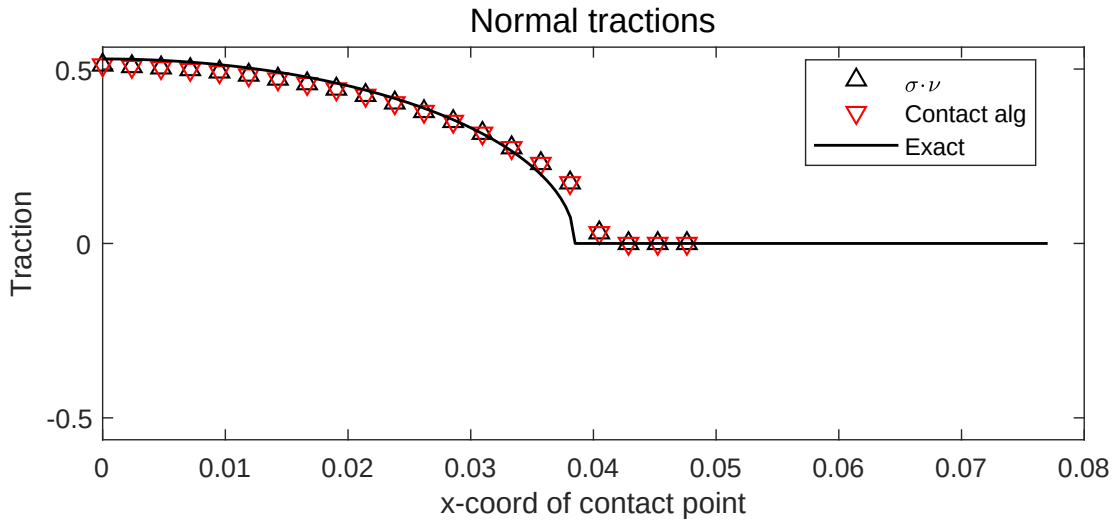

Figure 4.14: Contact pressure profile for half Hertzian contact problem

Next, the full Hertzian contact problem is solved using the proposed method. The numerical solution to the full problem with $\bar{\mathbf{u}} = \{0.0002, -0.0014\}$ is shown in Figure 4.15.

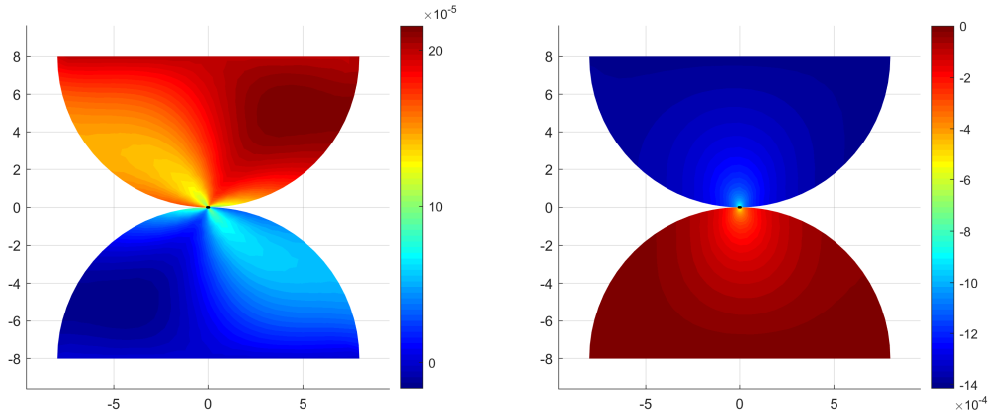

(a) (b)

Figure 4.15: (a) x-component and (b) y-component of displacement for the full Hertzian contact problem according to the proposed method

4.3.3 Thermomechanical contact between rectangular blocks

In this section, thermomechanical contact between rectangular blocks is examined. A version of this example was used in [47] to verify an enriched finite element method for thermomechanical contact. The geometry and uniform nodal arrangement for this problem are shown in Figure 4.16. Each block is a square of side length 1.0 meter. They are separated by a contact surface of frictional coefficient $\mu_f = 0.2$, resistivity coefficient $h_0 = 1.0$, resistivity exponent $P = 1.5$, and Vickers hardness $H_e = 3.0$ along a horizontal line through the origin. The block below the contact surface is fixed in both directions along its bottom surface and is fixed at a temperature change of 0 K. The top block has a prescribed displacement of $\mathbf{u} = \{0, \bar{u}_y\}$ along its top surface. The left and right sides of the blocks are traction-free and perfectly insulated. For both blocks, the Young's modulus and Poisson's ratio are $E = 0.07$MPa and $\nu = 0.3$, while the thermal conductivity and expansion coefficient are $\kappa = 150\text{J/m} \cdot \text{s} \cdot \text{K}$ and $\alpha_v = 1.0 \times 10^{-7}\text{K}^{-1}$. The normal and tangential penalty parameters are $\epsilon_N = \epsilon_T = 1.0 \times 10^4 E$.

Using this numerical example, the implementation of the pressure-dependent thermal

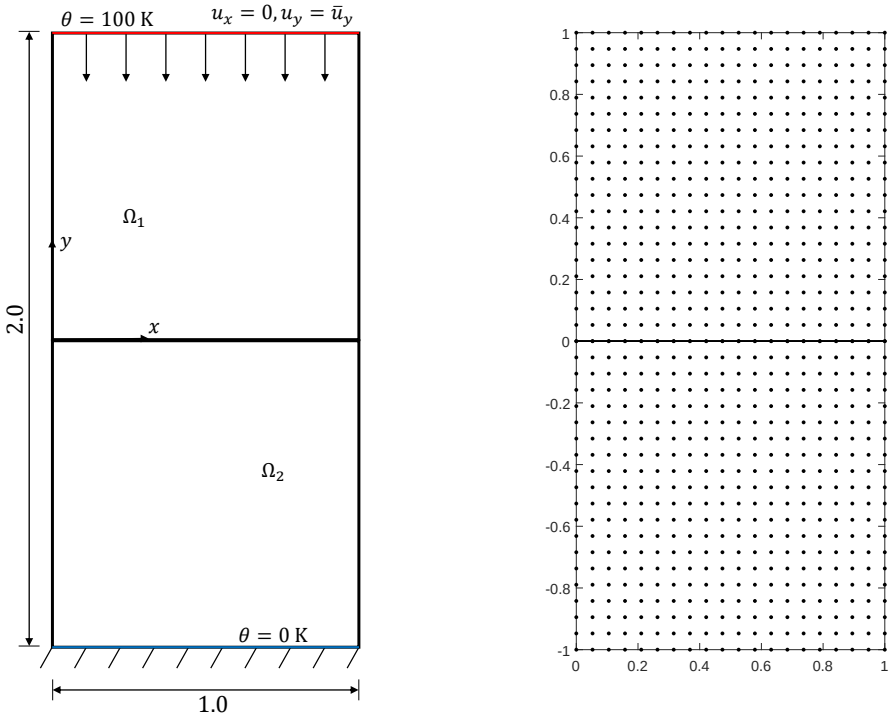

Figure 4.16: (a) Free-body diagram and (b) arrangement of collocation points for the problem of thermomechanical contact between rectangular blocks

contact model can be verified using an analytical solution for the temperature on either side of the contact interface. Specifically, for the pressure dependent model, the contact boundary temperatures are given in [47] and originally in [52] by

$$\begin{aligned} \theta^+ &= \frac{(\kappa + h(t_N))\theta_{\text{top}} + h(t_N)\theta_{\text{bottom}}}{\kappa + 2h(t_N)} \\ \theta^- &= \frac{(\kappa + h(t_N))\theta_{\text{bottom}} + h(t_N)\theta_{\text{top}}}{\kappa + 2h(t_N)} \end{aligned} \tag{4.71}$$

Here, θ^+ and θ^- are the temperatures on the edge above and below the contact surface respectively, θ_{top} and θ_{bottom} are the prescribed temperatures at the top and bottom edges of the entire domain respectively, and $h(t_N)$ is given by (4.22). To find the temperature profiles along the contact interface numerically, the proposed method is used with the uniform nodal arrangement shown in Figure 4.16 to solve the contact problem for various values of

prescribed displacement. Figure 4.17 shows contour plots of the components of displacement and temperature for $\bar{u}_y = -1.0 \times 10^{-3}$. The computed displacement and temperature fields in

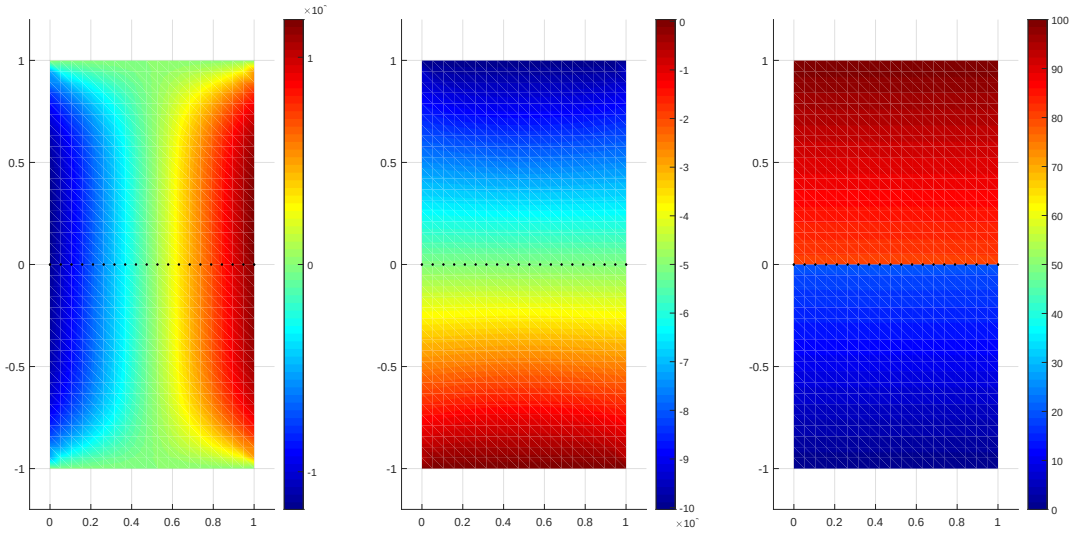

(a) (b) (c)

Figure 4.17: (a) x-component of displacement, (b) y-component of displacement, and (c) temperature for the problem of thermomechanical contact between rectangular blocks

Figure 4.17 are reasonable. As expected in the x-displacement field, the top and bottom edges are held fixed in the x-direction while the left and right sides experience a Poisson's effect. The y-component of displacement has an approximately constant slope in the y-direction, as expected since the two blocks have the same material properties. Any discrepancy from constant strain ϵ_{yy} can be explained by the thermal expansion of the top block. Finally, the temperature field has a jump at the contact interface but there is a temperature gradient across each block, reflecting the imperfect heat conduction across the interface modeled by (4.22).

Beyond these initial assurances, the numerical solution is verified by its agreement with the analytical solution for the temperature jump across the contact interface. The analytical temperatures along the contact interface are computed based on the computed contact pressure because an analytical solution based directly on prescribed displacement is unavailable.

Figure 4.18 shows that the temperature jump across the contact interface becomes smaller as the contact pressure increases because the increased contact pressure makes the surface more conductive, as expected. It also shows that the analytical temperature vs. contact

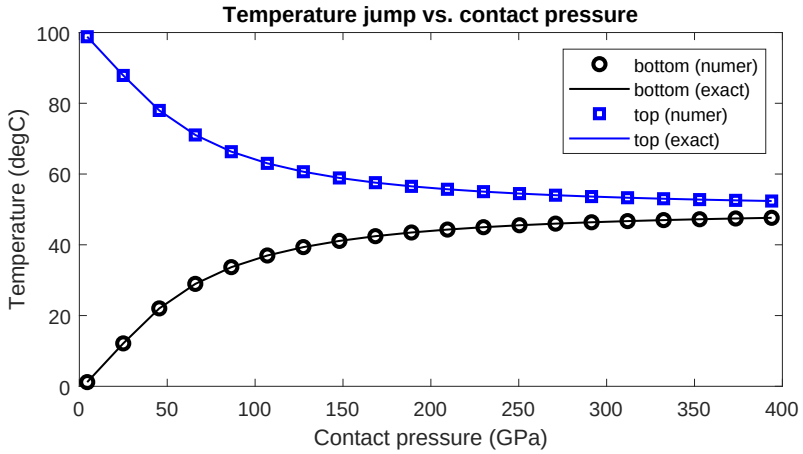

Figure 4.18: Temperature jump across contact interface for various values of contact pressure

pressure is visually indistinguishable from the computed solution. The maximum relative error between the analytical temperature and the computed temperature is

$$\frac{\max|\theta_{\text{exact}} - \theta_{\text{numer}}|}{\max|\theta_{\text{exact}}|} = 2.3 \times 10^{-4} \tag{4.72}$$

The numerical results from this section verify the implementation of the proposed method for thermomechanical contact. From the first example, it is clear that the method can accurately distinguish between stick and slip in the case of frictional contact. The second example (Hertzian contact) demonstrates that the proposed method can successfully match the analytical solution for a nontrivial contact pressure profile in the frictionless case and predict a reliable numerical solution of the governing equations in the frictional case. Based on the third example, the method can handle the additional nonlinearity of the thermal field, since the method accurately predicts the temperature jump across the contact interface for various levels of contact pressure. The results from this study are promising for future developments to the strong form meshfree collocation framework for thermomechanical contact.

Chapter 5

Conclusion

In this study, the strong form meshfree collocation method was used to solve higher-order and nonlinear PDEs arising in engineering applications. For both classes of problems, the proposed method produced reliable results that agreed with analytical or FEM solutions. The results of this study demonstrate that the proposed method has potential to be a viable alternative to the FEM for solving the higher-order and nonlinear PDEs that govern systems and processes of interest in engineering design. This study also elucidates the wide range of applications—from ocean circulation to thermomechanical contact—for which the proposed method is useful.

The first application considered in this study was the solution of higher-order PDEs in the context of wind-driven ocean circulation. To solve the fourth-order linear Stommel–Munk model for ocean circulation, the proposed method was modified using a weighted least squares approach to allow two boundary conditions to be applied simultaneously along the entire boundary. For each verification problem considered, the numerical results of the proposed method exhibited at least near-optimal and in some cases better than optimal convergence. Furthermore, local refinement was shown to improve the accuracy and convergence rate for both uniform grid and random nodal arrangements in the context of a problem whose exact solution had a difficult-to-capture high-gradient region in the form of a strong

western boundary layer. Finally, it was demonstrated that the proposed method successfully solved the fourth-order Stommel-Munk model on a polygon representing the Mediterranean Sea (a domain with complicated geometry), further implying the robustness and real-world applicability of the method. The proposed method's ability to predict wind-driven ocean circulation with reliable error convergence and on a domain with arbitrarily shaped boundaries bodes well for its ability to solve higher-order PDEs in other engineering contexts.

The second application considered in this study was the solution PDEs governing multibody thermomechanical contact, which are nonlinear due to the contact constraints. To solve these nonlinear equations, the proposed method was adapted to a staggered Newton-Raphson framework. In each example, the solution by the proposed method agreed with analytical or finite element solutions. In the inclined interface verification example, the method demonstrated a marked ability to distinguish between the stick and slip conditions and the contact traction profile agreed with results from commercial FEM software. The proposed method solution was shown to agree with the analytical solution for frictionless Hertzian contact, for which the contact pressure profile at the contact interface is nontrivial. Moreover, the method yielded a reasonable numerical solution for the Hertzian contact with friction. Finally, the method was shown to be accurate even with the additional nonlinearity introduced by the thermomechanical coupling, as evidenced by the example involving thermomechanical contact between rectangular blocks. Now that the proposed method has been verified for mechanical and thermomechanical contact, it can be used for more realistic applications, such as modeling of thermomechanical interactions in a nuclear fuel rod.

Future work will further explore the capability of the proposed method by solving the nonlinear stationary and the time-dependent quasi-geostrophic equations and contact problems with tighter coupling, large deformation, material nonlinearity, and time dependence. In particular, solving the nonlinear quasi-geostrophic equations presents the interesting challenge of combining the higher order and nonlinear capabilities of the current computational framework for the method. Expanding the capabilities of the contact framework presents

numerous challenges, including the additional material and geometric nonlinearities introduced, the need to implement a contact search algorithm and built-in adaptive refinement scheme, and the need to consider frictional heat sources and dynamic effects. More broadly, in light of the proposed method's potential for solving higher-order and nonlinear PDEs in a variety of contexts, opportunities abound for applying the method to wide-ranging engineering applications for which the method has particular advantages over more traditional computational methods.

Bibliography

[1] J.N. Reddy. *Theory and Analysis of Elastic Plates and Shells*. Boca Raton: CRC Press, 2007.

[2] J.W. Cahn and J.E. Hilliard. "Free energy of a nonuniform system. I. Interfacial free energy". In: *J. Chem. Phys.* 28 (1958), pp. 258–267.

[3] J.C. Simo and T.J.R. Hughes. *Computational Inelasticity*. New York: Springer-Verlag, 1998.

[4] A. Beel, T.Y. Kim, W. Jiang, and J.H. Song. "Strong form-based meshfree collocation method for wind-driven ocean circulation". In: *Computer Methods in Applied Mechanics and Engineering* Accepted (2019).

[5] Y.C. Yoon and J.H. Song. "Extended particle difference method for weak and strong discontinuity problems: part I. Derivation of the extended particle derivative approximation for the representation of weak and strong discontinuities". In: *Computational Mechanics* 53.6 (2014), pp. 1087–1103.

[6] P. Wriggers. *Computational Contact Mechanics*. Springer-Verlag, 2006.

[7] T. Belytschko, Y.Y. Lu, and L. Gu. "Element free Galerkin Methods". In: *International Journal for Numerical Methods in Engineering* 87 (1994), pp. 229–256.

[8] T. Rabczuk and T. Belytschko. "Cracking particles: a simplified meshfree method for arbitrary evolving cracks". In: *International Journal for Numerical Methods in Engineering* 61 (2004), pp. 2316–2343.

[9] T. Rabczuk, T. Belytschko, and S.P. Xiao. "Stable particle methods based on Lagrangian kernels". In: *Computer methods in applied mechanics and engineering* 193 (2004), pp. 1035–1063.

[10] C. Anitescu, Y. Jia, Y.Z. Zhang, and T. Rabczuk. "An isogeometric collocation method using superconvergent points". In: *Computer Methods in Applied Mechanics and Engineering* 284 (2015), pp. 1073–1097.

[11] S. Li and W.K. Liu. "Synchronized reproducing kernel interpolant via multiple wavelet expansion". In: *Computational Mechanics* 21 (1998), pp. 28–47.

[12] S. Li and W.K. Liu. "Reproducing kernel hierarchical partition of unity, Part I-formulation and theory". In: *International Journal for Numerical Methods in Engineering* 45 (1999), pp. 251–288.

[13] S. Li and W.K. Liu. "Meshfree and particle methods and their applications". In: *Applied Mechanics Reviews* 55 (2002), pp. 1–34.

[14] D.W. Kim and Y. Kim. "Point collocation method using the fast moving least-square reproducing kernel approximation". In: *International Journal for Numerical Methods in Engineering* 56.10 (2003), pp. 1445–1464.

[15] M. Hillman and J.S. Chen. "An accelerated, convergent, and stable nodal integration in Galerkin meshfree methods for linear and nonlinear mechanics". In: *International Journal for Numerical Methods in Engineering* 107 (2016), pp. 603–630.

[16] S.H. Lee and Y.C. Yoon. "Meshfree point collocation method for elasticity and crack problems". In: *International Journal for Numerical Methods in Engineering* 61.1 (2004), pp. 22–48.

[17] D.W. Kim, W.K. Liu, Y.C. Yoon, T. Belytschko, and S.H. Lee. "Meshfree point collocation method with intrinsic enrichment for interface problems". In: *Computational Mechanics* 40 (2007), pp. 1037–1052.

[18] D.W. Kim, Y.C., Yoon, W.K. Liu, and T. Belytschko. "Extrinsic meshfree approximation using asymptotic expansion for interfacial discontinuity of derivative". In: *Journal of Computational Physics* 221 (2007), pp. 370–394.

[19] Y.C. Yoon and J.H. Song. "Extended particle difference method for weak and strong discontinuity problems: part II. Formulations and applications for various interfacial singularity problems". In: *Computational Mechanics* 53.6 (2014), pp. 1105–1128.

[20] Y.C. Yoon and J.H. Song. "Extended particle difference method for moving boundary problems". In: *Computational Mechanics* 54.3 (2014), pp. 723–743.

[21] J.H. Song, Y. Fu, T.Y. Kim, Y.C. Yoon, J. G. Michopoulos, and T. Rabczuk. "Phase field simulations of coupled microstructure solidification problems via the strong form particle difference method". In: *International Journal of Mechanics and Materials in Design* 14 (2018), pp. 491–509.

[22] Y. Fu, J.G. Michopoulos, and J.H. Song. "Bridging the multi phase-field and molecular dynamics models for the solidification of nano-crystals". In: *Journal of Computational Science* 20 (2017), pp. 187–197.

[23] A. Almasi, A. Beel, T.Y. Kim, J.G. Michopoulos, and J.H. Song. "Strong form collocation method for solidification and mechanical analysis of polycristaline materials". In: *ASCE Journal of Engineering Mechanics* Accepted (2019).

[24] Y.C. Yoon, P. Schaefferkoetter, T. Rabczuk, and J.H. Song. "New strong formulation for material nonlinear problems based on the particle difference method". In: *Engineering Analysis with Boundary Elements* 98 (2019), pp. 310–327.

[25] H.Y. Hu, J.S. Chen, and S.W. Chi. "Perturbation and stability analysis of strong form collocation with reproducing kernel approximation". In: *International Journal for Numerical Methods in Engineering* 88 (2011), pp. 157–179.

[26] H.A. Dijkstra. *Nonlinear Physical Oceanography: A Dynamical Systems Approach to the Large Scale Ocean Circulation and El Niño*. Springer-Verlag, 2005.

[27] G.K. Vallis. *Atmosphere and Ocean Fluid Dynamics: Fundamentals and Large-scale Circulation*. Cambridge University Press, 2006.

[28] J. Pedlosky. *Geophysical Fluid Dynamics*. Springer-Verlag, 1992.

[29] O. San, A.E. Staples, Z. Wang, and T. Iliescu. "Approximate deconvolution large eddy simulation of a barotropic ocean circulation model". In: *Ocean Modelling* 40 (2011), pp. 120–132.

[30] T.D. Ringler, J. Thuburn, J.B. Klemp, and W.C. Skamarock. "A unified approach to energy conservation and potential vorticity dynamics for arbitrary-structured C-grids". In: *Journal of Computational Physics* 229 (2010), pp. 3065–3090.

[31] Q. Chen, T.D. Ringler, and M. Gunzburger. "A co-volume scheme for the rotating shallow water equations on conforming non-orthogonal grids". In: *Journal of Computational Physics* 240 (2013), pp. 174–197.

[32] P.G. Myers and A.J. Weaver. "A diagnostic barotropic finite-element ocean circulation model". In: *Journal of Atmospheric and Oceanic Technology* 12 (1995), pp. 511–526.

[33] J.M. Cascón, G.C. Garcia, and R. Rodriguez. "A priori and a posteriori error analysis for a large-scale ocean circulation finite element model". In: *Computer Methods in Applied Mechanics and Engineering* 192 (2003), pp. 5305–5327.

[34] G.J. Fix. "Finite element models for ocean circulation problems". In: *SIAM Journal on Applied Mathematics* 29.3 (1975), pp. 371–387.

[35] E.L. Foster, T. Iliescu, and Z. Wang. "A finite element discretization of the streamfunction formulation of the stationary quasi-geostrophic equations of the ocean". In: *Computer Methods in Applied Mechanics and Engineering* 261 (2013), pp. 105–117.

[36] T.-Y. Kim, E.-J. Park, and D. Shin. "A C^0-discontinuous Galerkin method for the stationary quasi-geostrophic equations of the ocean". In: *Computer Methods in Applied Mechanics and Engineering* 300 (2016), pp. 225–244.

[37] D. Kim, T.-Y. Kim, E.-J. Park, and D. Shin. "Error estimates of B-splined based finite-element methods for the stationary quasi-geostrophic equations of the ocean". In: *Computer Methods in Applied Mechanics and Engineering* 335 (2018), pp. 225–272.

[38] N. Rotundo, T.-Y. Kim, W.-L. Heltai, and E. Fried. "Error analysis of a B-Spline Based finite-element method for modeling wind-driven ocean circulation". In: *Journal of Scientific Computing* 69.1 (2016), pp. 430–459.

[39] T.-Y. Kim, T. Iliescu, and E. Fried. "B-spline based finite-element method for the stationary quasi-geostrophic equations of the ocean". In: *Computer Methods in Applied Mechanics and Engineering* 286 (2015), pp. 168–191.

[40] I. Al Balushi, W. Jiang, G. Tsogtgerel, and T.-Y. Kim. "Adaptivity of a B-spline based finite-element method for modeling wind-driven ocean circulation". In: *Computer Methods in Applied Mechanics and Engineering* 332 (2018), pp. 1–24.

[41] W. Jiang and T.-Y. Kim. "Spline-based finite-element method for the stationary quasi-geostrophic equations on arbitrary shaped coastal boundaries". In: *Computer Methods in Applied Mechanics and Engineering* 299 (2016), pp. 144–160.

[42] T.J.R. Hughes, J.A. Cottrell, and S.Y. Bazilevs. "Isogeometric analysis: CAD, finite elements, NURBS, exact geometry and mesh refinement". In: *Computer Methods in Applied Mechanics and Engineering* 194 (2005), pp. 4135–4195.

[43] K. Höllig. *Finite Element Methods with B-splines*. Philadelphia: SIAM, 2003.

[44] Y. Bazilevs and T.J.R. Hughes. "Weak imposition of Dirichlet boundary conditions in fluid mechanics". In: *Computers & Fluids* 36.1 (2007), pp. 12–26.

[45] B.W. Spencer, R.L. Williamson, D.S. Stafford, S.R. Novascone, J.D. Hales, and G. Pastore. "3D modeling of missing pellet surface defects in BWR fuel". In: *Nuclear Engineering and Design* 307 (2016), pp. 155–171.

[46] R.L. Williamson, J.D. Hales, S.R. Novascone, M.R. Tonks, D.R. Gaston, C.J. Permann, D. Andrs, and R.C. Martineau. "Multidimensional multiphysics simulation of nuclear fuel behavior". In: *Journal of Nuclear Materials* 423 (2012), pp. 149–163.

[47] A.R. Khoei and B. Bahmani. "Application of an enriched FEM technique in thermo-mechanical contact problems". In: *Computational Mechanics* 62.5 (2018), pp. 1127–1154.

[48] S.R. Novascone, B.W. Spencer, J.D. Hales, and R.L. Williamson. "Evaluation of coupling approaches for thermomechanical simulations". In: *Nuclear Engineering and Design* 295 (2015), pp. 910–921.

[49] C. Danowski, V. Gravemeier, L. Yoshihara, and W.A. Wall. "A monolithic computational approach to thermo-structure interaction". In: *International Journal for Numerical Methods in Engineering* 95 (2013), pp. 1053–1078.

[50] C. Farhat, K.C. Park, and Y. Dubois-Pelerin. "An unconditionally stable staggered algorithm for transient finite element analysis of coupled thermoelastic problems". In: *Computer Methods in Applied Mechanics and Engineering* 85 (1991), pp. 349–365.

[51] P. Papadopoulos and R.L. Taylor. "A mixed formulation for the finite element solution of contact problems". In: *Computer Methods in Applied Mechanics and Engineering* 94 (1992), pp. 373–389.

[52] P. Wriggers and C. Miehe. "Contact constraints within coupled thermomechanical analysis — a finite element model". In: *Computer Methods in Applied Mechanics and Engineering* 113 (1994), pp. 301–319.

[53] Y. Maday, C. Mavriplis, and A. Patera. "Nonconforming mortar element methods: Application to spectral discretizations". In: *Domain Decomposition Methods, SIAM* (1989), pp. 392–418.

[54] T.W. McDevitt and T.A. Laursen. "A mortar-finite element formulation for frictional contact problems". In: *International Journal for Numerical Methods in Engineering* 48 (2000), pp. 1525–1547.

[55] B. Yang, T.A. Laursen, and X. Meng. "Two dimensional mortar contact methods for large deformation frictional sliding". In: *International journal for numerical methods in engineering* 62 (2005), pp. 1183–1225.

[56] T.Y. Kim, J. Dolbow, and T.A. Laursen. "A mortared finite element method for frictional contact on arbitrary interfaces". In: *Computational Mechanics* 39 (2007), pp. 223–235.

[57] F.B. Belgacem, P. Hild, and P. Laborde. "Approximation of the unilateral contact problem by the mortar finite element method". In: *Comptes Rendus de l'Academie des Sciences Series I Mathematics* 324 (1997), pp. 123–127.

[58] F.B. Belgacem, P. Hild, and P. Laborde. "The mortar finite element method for contact problems". In: *Mathematical and Computer Modelling* 28 (1998), pp. 263–272.

[59] M.A. Puso and T.A. Laursen. "A mortar segment-to-segment contact method for large deformation solid mechanics". In: *Computer methods in applied mechanics and engineering* 193 (2004), pp. 601–629.

[60] J.H. Friedman, J. Bentley, and R.A. Finkel. "An algorithm for finding best matches in logarithmic time". In: *ACM Trans. Math. Software 3* 3 (1977), pp. 209–226.

[61] D.W. Kim and H.K. Kim. "Point collocation method based on the FMLSRK approximation for electromagnetic field analysis". In: *IEEE Transactions on Magnetics* 40.2 (2004), pp. 1029–1032.

[62] C. Geuzaine and J.-F. Remacle. "Gmsh: a three-dimensional finite element mesh generator with built-in pre- and post-processing facilities". In: *International Journal for Numerical Methods in Engineering* 79.11 (2009), pp. 1309–1331.

[63] J.S. Chen, W. Hu, and H.Y. Hu. "Reproducing kernel enhanced local radial basis collocation method". In: *International Journal for Numerical Methods in Engineering* 75 (2007), pp. 600–627.

[64] T.A. Laursen. *Computational contact and impact mechanics: fundamentals of modeling interfacial phenomena in nonlinear finite element analysis*. Berlin: Springer-Verlag, 2003.

[65] K.L. Johnson. *Contact Mechanics*. Cambridge University Press, 1985.